LAWRENCE
LIVERMORE
NATIONAL
LABORATORY

LLNL-TR-534132

Final Report: Detection and Characterization of Underground Facilities by Stochastic Inversion and Modeling of Data from the New Generation of Synthetic Aperture Satellites

W. Foxall, C. Cunningham, R. Mellors, D. Templeton, K. Dyer, J. White

February 29, 2012

Disclaimer

This work performed under the auspices of the U.S. Department of Energy by Lawrence Livermore National Laboratory under Contract DE-AC52-07NA27344.

LAWRENCE
LIVERMORE
NATIONAL
LABORATORY

LLNL-TR-534132

Final Report: Detection and Characterization of Underground Facilities by Stochastic Inversion and Modeling of Data from the New Generation of Synthetic Aperture Satellites

W. Foxall, C. Cunningham, R. Mellors, D. Templeton, K. Dyer, J. White

February 29, 2012

Disclaimer

This work performed under the auspices of the U.S. Department of Energy by Lawrence Livermore National Laboratory under Contract DE-AC52-07NA27344.

Final Report

LL09-InSARinv-PD06

Detection and Characterization of Underground Facilities by Stochastic Inversion and Modeling of InSAR data from the New Generation of Synthetic Aperture Radar Satellites

W. Foxall, C. Cunningham, R. Mellors, D, Templeton, K. Dyer, and J. White

Lawrence Livermore National Laboratory

---

1. Introduction

Many clandestine development and production activities can be conducted underground to evade surveillance. The purpose of the study reported here was to develop a technique to detect underground facilities by broad-area search and then to characterize the facilities by inversion of the collected data. This would enable constraints to be placed on the types of activities that would be feasible at each underground site, providing a basis the design of targeted surveillance and analysis for more complete characterization.

Excavation of underground cavities causes deformation in the host material and overburden that produces displacements at the ground surface. Such displacements are often measurable by a variety of surveying or geodetic techniques. One measurement technique, Interferometric Synthetic Aperture Radar (InSAR), uses data from satellite-borne (or airborne) synthetic aperture radars SARs) and so is ideal for detecting and measuring surface displacements in denied access regions. Depending on the radar frequency and the acquisition mode and the surface conditions, displacement maps derived from SAR interferograms can provide millimeter- to centimeter-level measurement accuracy on regional and local scales at spatial resolution of ~1-10 m. Relatively low-resolution (~20 m, say) maps covering large regions can be used for broad-area detection, while finer resolutions (~1 m) can be used to image details of displacement fields over targeted small areas.

Surface displacements are generally expected to be largest during or a relatively short time after active excavation, but, depending on the material properties, measurable displacement may continue at a decreasing rate for a considerable time after completion. For a given excavated volume in a given geological setting, the amplitude of the surface displacements decreases as the depth of excavation increases, while the area of the discernable displacement pattern increases. Therefore, the ability to detect evidence for an underground facility using InSAR depends on the displacement sensitivity and spatial

resolution of the interferogram, as well as on the size and depth of the facility and the time since its completion.

The methodology development described in this report focuses on the exploitation of synthetic aperture radar data that are available commercially from a number of satellite missions. Development of the method involves three components: (1) Evaluation of the capability of InSAR to detect and characterize underground facilities ; (2) inversion of InSAR data to infer the location, depth, shape and volume of a subsurface facility; and (3) evaluation and selection of suitable geomechanical forward models to use in the inversion.

We adapted LLNL's general-purpose Bayesian Markov Chain-Monte Carlo procedure, the "Stochastic Engine" (SE), to carry out inversions to characterize subsurface void geometries. The SE performs forward simulations for a large number of trial source models to identify the set of models that are consistent with the observations and prior constraints. The inverse solution produced by this kind of stochastic method is a posterior probability density function (pdf) over alternative models, which forms an appropriate input to risk-based decision analyses to evaluate subsequent response strategies.

One major advantage of a stochastic inversion approach is its ability to deal with complex, non-linear forward models employing empirical, analytical or numerical methods. However, while a geomechanical model must incorporate adequate physics to enable sufficiently accurate prediction of surface displacements, it must also be computationally fast enough to render the large number of forward realizations needed in stochastic inversion feasible. This latter requirement prompted us first to investigate computationally efficient empirical relations and closed-form analytical solutions. However, our evaluation revealed severe limitations in the ability of existing empirical and analytical forms to predict deformations from underground cavities with an accuracy consistent with the potential resolution and precision of InSAR data. We followed two approaches to overcoming these limitations. The first was to develop a new analytical solution for a 3D cavity excavated in an elastic half-space. The second was to adapt a fast parallelized finite element method to the SE and evaluate the feasibility of using in the stochastic inversion.

To date we have demonstrated the ability of InSAR to detect underground facilities and measure the associated surface displacements by mapping surface deformations that track the excavation of the Los Angeles Metro system. The Stochastic Engine implementation has been completed and undergone functional testing. We completed a comprehensive evaluation of existing geomechanical models, and have completed the development of the first part of a new approximate analytical solution for a circular 3D tunnel buried in an elastic half space. We have developed an automated script that generates finite element mesh realizations in just a few seconds given input parameters describing excavation geometries. This and the excellent parallel scalability of the finite element code suggest that this modeling approach should be feasible. We have tested an interface between the finite element code and the SE for relatively simple subsurface sources, but testing its application to finite void sources has not yet been completed.

2. InSAR

2.1 Overview of the InSAR Method

2.1.1 Characteristics of Synthetic Aperture Radar: Synthetic Aperture Radar (SAR) is an active imaging technique that uses microwave-length electromagnetic energy to create back-scatter images of the earth's surface from a moving satellite-borne or airborne sideways-looking antenna. Images can be collected during the night or day and the signal can penetrate clouds. The radar records the full complex signals (modulus and phase) of reflections (echos) from the ground surface. Unlike optical data, SAR data requires processing to generate an image. In basic "strip map" mode the radar illuminates a continuous swath on the ground, but there are several other modes (e.g. ScanSAR and Spotlight) with differing characteristics. For details see Curlander and McDonough (1991).

In this study we focus on SAR data that are commercially available. Basic specifications for the current generation of commercial and dual-use satellite SARs are given in Table 1. The current SARs operate at either C- or X-band; archived data are available from past C- and L-band missions, two of which (ENVISAT and ALOS) ended recently. Note that image resolution is generally somewhat higher in the azimuth direction, and that final image resolution also depends on smoothing and filtering during processing. Reflection strength, phase, and polarization depend mainly on the radar acquisition geometry, and the roughness and electromagnetic properties of the ground surface. The amplitude and phase returned by each resolution element (pixel) on the ground are each the average of those from all the reflecting surfaces (scatterers) in the pixel. A special case is a "point scatterer" that has an appropriate geometry (ideally a 3D corner reflector) to reflect back a very strong signal, and thus makes the dominant contribution to the phase and amplitude of the pixel. Point scatters are most commonly man-made structures but can also occur naturally. The phase of the radar signal is slightly altered by variations in tropospheric water vapor content, and also slightly by ionospheric conditions, the effects of which are more pronounced at longer wavelengths (L-band).

2.1.2 InSAR Processing: InSAR uses the difference in phase between two SAR scenes of the same area acquired at two different times but from approximately the same orbital position to detect displacements of the ground surface. The difference between the phases of the two radar returns from the same resolution element (Figure 1) is proportional to any change in the slant distance (range) from the ground to the radar caused by coherent displacement of the element that occurs during the time interval between the orbits, and to the ground elevation. The topographic contribution is subtracted using a digital elevation model (DEM) or additional repeat orbits. Successful InSAR processing requires that the two images be aligned at the pixel level, and that in both images the relative phase change between adjacent pixels is similar; i.e. the phases remain coherent (correlated). The coherence can be destroyed by any process that disturbs the distribution of sub-pixel scatterers, such as vegetation growth or plowing, in which case temporal decorrelation occurs and the measurement is meaningless.

Table 1: Current SAR Satellites

	TerraSAR (Germany)	**RADARSAT-2** (Canada)	**COSMO-Skymed**[1] (Italy)
Launch	6/07	12/07	6/07, 12/07
Band	X	C	X
Resolution (m): SL[2]	1	3	1
SM	3	10	3
SS	16	60	30
Revisit (days)	11	24	16 (each satellite)
Swath SL	5	20	10
width (km): SM	30	50-100	40
SS	100	300	100
Right/left antenna looking	R/L	R/L	R/L
Displacement prec. (approx, mm)	1	3	1

(1) Constellation of four satellites
(2) **SL** - spotlight; **SM** – strip map; **SS** – ScanSAR

The relative phases between pixels also depend on the acquisition geometry relative to the surface topography, atmospheric effects, variations in surface electromagnetic response, and system noise. If the satellite position and topography are known with sufficient accuracy, geometric corrections can be calculated and removed. The separation between the two orbital positions is termed the spatial baseline (B in Figure 1). The maximum (critical) baseline allowed is generally a few kilometers or less, depending on the radar frequency and viewing geometry. The phase coherence between the two SAR scenes - and hence the interferogram signal-to-noise ratio (SNR) - degrades as the baseline becomes larger, and is completely lost beyond the critical baseline. This is termed spatial or baseline decorrelation. The sensitivity to topography also increases with increasing baseline.

The corrected pixel-by-pixel phase changes are mapped over the entire radar scene to produce an interferogram. As the differencing operation is performed on two complex numbers and the difference converted to a real number representing phase using the inverse tangent, the result is known only *modulo*(2π) (phase wrapping). In most cases the interferogram image must be unwrapped to map absolute phase differences. Phase unwrapping can be difficult when large displacements are imaged or substantial portion of the interferogram are uncorrelated.

The interferogram contains phase contributions from surface displacement, atmospheric effects, and errors from inadequately known satellite orbits or topography, processing or unwrapping artifacts, and system noise. In our application, the surface displacements are the signal of interest, so that the other contributions are considered noise. Unfortunately, in many cases the amplitude of the noise is expected to be

comparable to that of the expected signals, so that a large part of the processing effort lies in estimating and removing errors.

2.2 InSAR Time Series Analysis and Error Estimation

Time series analysis and error estimation utilizes multiple interferograms, each covering a different time period. Each of error the error types mentioned above has different spatial and temporal characteristics, and the differences can be exploited to isolate and then remove each error signal. System noise is expected to be random both spatially and temporally and therefore can be reduced by spatial and/or temporal averaging. Incorrect orbit estimates cause errors with long spatial wavelengths, but are random in time, while errors in topography are generally assumed to be more significant at high spatial wavelengths and are constant in time. Atmospheric effects tend to vary both temporally and spatially, although a layered atmosphere and orographic effects may generate atmospheric signals at longer spatial wavelengths that correlate with topography.

Several different approaches have been developed to remove errors using multiple interferograms, and this remains an active area of research. The simplest method is to simply average, or stack the interferograms. If the noise is random and normally distributed, stacking is expected to reduce the noise by a factor of $\sqrt{N}$, where N is the number of interferograms. However, most errors in interferograms are not normally distributed and so stacking is not always effective. For larger numbers of interferograms (> 20), stacking does tend to improve the SNR for temporally random thermal and atmospheric noise. An iterative approach in which individual interferograms are compared with the initial stack, can be effective in identifying interferograms and the associated SAR scenes that are heavily contaminated by atmospheric effects. The advantage of simple stacking is that no assumptions about the signal characteristics are required. Typical errors in range change measurements after stacking a sufficient number of images are on the order of one cm in areas with good coherence and moderate topography.

Another approach, Short Baseline Subset (SBAS), uses only stacks of interferograms with short baselines that can be successfully unwrapped prior to application of a singular value decomposition time-series algorithm (Berardino et al., 2002). This both reduces the sensitivity to topographic error and increases the coherence. Typically, one pixel is designated as stable and a combined filtering/inverse approach is used to extract the signal and distinguish it from other contributions. A disadvantage is that signals that are strongly non-linear in time are often poorly resolved. Range change resolution on the order of mm has been achieved with this method.

A third approach [Ferretti et al., 2000] attempts to define specific pixels whose phase is dominated by a single strong scatterer. These points, known as persistent scatterers (PS), remain coherent with respect to other persistent scatterers in the scene, even at long baselines and over long time periods. Once identified, these points can be used as a basis for a filtering and inversion scheme to resolve displacements. This PSInSAR method does not require unwrapping but does require identification of a sufficient density of PS, in which case better resolution can often be achieved than with SBAS, since more interferograms can be used. Recently, Ferretti et al. (2011) have introduced a technique that combines point and distributed scatterers. This technique recovers some of the continuous spatial resolution of conventional InSAR and is more effective in rural areas than PSInSAR.

2.3 Detection and Modeling of Known Tunnels Using InSAR

Tunnels under construction have been imaged by InSAR in a few of previous studies, including subway tunnels in London (Buckley et al., 2005). InSAR has also been used to map and characterize subsidence due to mining operations (e.g. Perski, 1998; Foxall et al., 1998). We selected tunnels excavated in the Los Angeles Basin for an evaluation of the ability of InSAR to detect and measure tunneling-induced surface displacements.

2.3.1 InSAR Processing and Analysis for Los Angeles: Segments of the dual-tunnel Los Angeles "Red Line" subway system were dug during the time period 1985-1996. The diameters of the twin tunnels are 6.3 m. Most of the tunnel segments were excavated in the sediments and alluvium of the Los Angeles basin, but one segment extended under the Santa Monica Mountains in consolidated rock. (Stirbys et al., 1999). During construction, subsidence, cracks, and sinkholes were reported in numerous places, notably Hollywood Boulevard and the Hollywood Freeway. Some of the subsidence was reported to be as much as 9 inches (13.5 cm). Most of the construction was under urban areas with the exception of the Santa Monica Mountains, which are rugged, vegetated and sparsely populated.

Thirty-nine standard resolution SAR scenes from the European Space Agency ERS1 and ERS2 C-band satellites were downloaded from the WINSAR consortium repository and used to form the InSAR pairs specified in Table 2 and Figure 2. The satellites operated in a sun-synchronous polar orbit with a repeat cycle of 35 days. The nominal swath width of the SARs was 100 km and the mid-swath incidence angle was 23 degrees. We processed the data using the commercial GAMMA software package and a US National Elevation Dataset DEM to remove topography. Because the satellites did not have the capability for precise location onboard, we used precise orbits based on altimetry data and gravity field modeling (Scharoo et al., 1998) to calculate spatial baselines. All of the scenes were aligned to a master image (951207) (Figure 2). At this stage we eliminated several interferograms due to missing data lines or excessive spatial or temporal baselines. Pixels having a phase coherence of less than 0.18 were masked out in the remaining interferograms, and their geolocationwere verified against an optical image from Google Earth (Figure 3).

Initial examination indicated a line of subsidence along the tunnel on individual interferograms spanning the construction time period, as can be seen in Figure 4. However, linear streaks of decorrelation are also evident, which made the signal difficult to positively identify in some locations. Interferograms covering time periods after tunnel construction was completed do not show similar displacement signatures, indicating that the subsidence occurred during tunnel construction.

Apparent uplift can be seen along the tunnel path in interferograms that cover time periods immediately after tunnel excavation. This is occurred first and is most obvious along the Wilshire segment, but also became apparent on the Vermont section. This uplift, which is expressed as a decrease in slant range change, is more spatially diffuse than the initial subsidence signal, which suggests that it may be due to the poroelastic effect caused by ground water flow induced by excavation. Some of these later interferograms also show significant deformation north of the Santa Monica mountains caused by the January 17, 1994 Northridge earthquake. The deformation from

the earthquake had a long spatial wavelength, so it is easy to distinguish from the tunnel signature and can be removed by high-pass filtering.

Stacking interferograms that spanned the 1993-1995 time period improved the signal, as can be seen in Figure 5. The stacks were constructed by summing all the interferograms within that period pixel by pixel and dividing by the total number of images. Low-coherence pixels were masked out and those that are masked on more than 50% of the interferograms are not included in the stack. The resulting displacement signature exactly matches the known tunnel path; in particular, the northward curve towards the Santa Monica mountains west of the Hollywood-Highland station is clearly visible on the stacked image but indistinguishable on the individual interferograms. In comparison, post-construction stacks show no indication of the signal, which indicates that the deformation signal corresponds to tunnel construction.

We attempted to improve the signal by additional high-pass filtering to eliminate residual atmospheric effects, and also by subtracting a low-pass filtered signal from the original to remove long-wavelength artifacts. None of these efforts proved particularly effective; because the tunnel signal is weak, most of the filtering either eliminated the signal or introduced high-frequency filter artifact noise. The map of coherent hits per pixel (Figure 6, *bottom*) reveals that the tunnel location suffers higher decorrelation than adjacent pixels, but the standard deviation (Figure 6, *top*) indicates that the resulting loss of data does not produce any artifacts, indicating that the signal is likely to be real. Furthermore, the zone (linear in our case) of higher decorrelation may also serve as useful means of detection.

As a check of the results, we compared ground-based measurements of the tunnel subsidence with the InSAR data. Figure 7 shows InSAR displacement rate profiles perpendicular to the tunnel axis. The subsidence signature is discernable, but its magnitude is close to the one standard deviation noise levels along the profiles. Ground-based measurement profiles along the tunnel are shown in Figure 8 (URS Corp., personal communication). Figure 9 compares the InSAR and ground-based profiles along the tunnel axis, and illustrates that the spatial variability in the precise ground-based leveling measurements is similar to that of the InSAR data.

2.3.2 Application of Advanced InSAR Techniques: In addition to simple stacking, we also tested an SBAS technique and carried out PS analysis. SBAS attempts to invert directly for the displacement rate as a function of time, and the time resolution is determined by the times of acquisition of the available SAR scenes (Berardino et al. 2002). Since no data for the Los Angeles scene during the main period of tunnel construction in 1994 are available from the WINSAR archive, the SBAS results are similar in resolution to the raw stacks.

We carried out PS analysis using the GAMMA Interferometric Point Target Analysis (IPTA) software package. The urban area of the Los Angeles basin is rich in scatterers and a clear image of the zones of the subsidence and uplift was obtained (Figure 10). In the analysis we assumed linear deformation rates and estimated and removed corrections for atmospheric, baseline, and topography. Linear displacement time series, such as those shown on the insets in Figure 10, are well resolved. The large area of predominantly subsidence towards the west side of the figure is caused by fluid extraction from an active oilfield. The subsidence over the tunnel excavation is fairly well defined but is not as prominent as the fluid-related signals. This may be due to non-linear behavior in the displacements combined with the poor coverage during the main

construction period. As the PS algorithm attempts to match the observed time series with a linear fit, strongly non-linear signals will provide unpredictable results if the data are noisy. Another possible explanation is that subsidence over the tunnel was spatially variable on scales on the order of meters, as indicated both the InSAR and ground-based measurements in Figures 8 and 9, which might be attributable to differences in the responses to the subsidence of the buildings that act as permanent scatterers due to lateral variations in near-surface material properties.

Table 2. Parameters of ERS1 and ERS2 SAR interferometric pairs

date1	date2	bperp	year1	year2	time
920601	950719	-127.79	1992.42	1995.55	3.13
920601	951206	-22.85	1992.42	1995.93	3.51
920601	951207	-175.87	1992.42	1995.93	3.52
920601	960110	-60.37	1992.42	1996.03	3.61
920914	951102	111.03	1992.71	1995.84	3.13
920914	960214	72.95	1992.71	1996.12	3.42
920914	960215	94.11	1992.71	1996.13	3.42
921019	950405	-68.89	1992.8	1995.26	2.46
921019	950614	68.29	1992.8	1995.45	2.65
921019	951207	214.57	1992.8	1995.93	3.13
921019	960912	-6.24	1992.8	1996.7	3.9
921123	951206	-115.55	1992.9	1995.93	3.03
921123	960704	10.59	1992.9	1996.51	3.61
921123	961017	101.97	1992.9	1996.8	3.9
921228	930830	113.07	1992.99	1993.66	0.67
921228	960529	93.65	1992.99	1996.41	3.42
930308	971106	-19.96	1993.18	1997.85	4.67
930308	971211	53.11	1993.18	1997.95	4.76
930830	950405	98.19	1993.66	1995.26	1.6
930830	960529	-19.39	1993.66	1996.41	2.75
930830	980219	13.84	1993.66	1998.14	4.47
931004	950614	-81.81	1993.76	1995.45	1.69
931004	950719	114.03	1993.76	1995.55	1.79
931004	950823	13.04	1993.76	1995.64	1.88
931004	970306	20.99	1993.76	1997.18	3.42
931108	950719	-99.55	1993.85	1995.55	1.69
931108	951206	1.89	1993.85	1995.93	2.08
931108	951207	-149.44	1993.85	1995.93	2.08
931108	960110	-27.73	1993.85	1996.03	2.17
931108	980430	52.16	1993.85	1998.33	4.47
950405	960529	-117.6	1995.26	1996.41	1.15
950405	960912	62.65	1995.26	1996.7	1.44
950405	980115	-0.25	1995.26	1998.04	2.78
950614	960912	-74.51	1995.45	1996.7	1.25
950614	961226	-1.39	1995.45	1996.99	1.54
950614	970306	102.93	1995.45	1997.18	1.73
950614	970515	134.34	1995.45	1997.37	1.92
950719	951206	101.72	1995.55	1995.93	0.38
950823	950927	201.71	1995.64	1995.74	0.1
950823	970306	7.36	1995.64	1997.18	1.53
950823	970515	38.8	1995.64	1997.37	1.73

950823	970619	-61.44	1995.64	1997.47	1.82
950823	970724	63.77	1995.64	1997.56	1.92
950927	951207	-150.96	1995.74	1995.93	0.19
950927	970306	-194.4	1995.74	1997.18	1.44
950927	970724	-137.96	1995.74	1997.56	1.82
951102	960215	-16.95	1995.84	1996.13	0.29
951207	960912	-220.86	1995.93	1996.7	0.77
951207	961226	-147.74	1995.93	1996.99	1.05
951207	970306	-43.42	1995.93	1997.18	1.24
951207	970515	-11.97	1995.93	1997.37	1.44
951207	970619	-112.2	1995.93	1997.47	1.53
951207	970724	12.96	1995.93	1997.56	1.63
951207	971002	240.74	1995.93	1997.75	1.82
951207	980430	201.27	1995.93	1998.33	2.39
951207	980813	0.06	1995.93	1998.62	2.68
951207	981126	-179.15	1995.93	1998.9	2.97
951207	990311	-104.23	1995.93	1999.19	3.26
960214	970410	-14.77	1996.12	1997.27	1.15
960529	981022	-27.59	1996.41	1998.81	2.4
960529	990204	-61.04	1996.41	1999.1	2.68
960704	971002	-36.39	1996.51	1997.75	1.24
961017	970828	4.62	1996.8	1997.66	0.86
961017	990729	24.83	1996.8	1999.58	2.78
961226	981126	-31.41	1996.99	1998.9	1.92
980115	000608	7.34	1998.04	2000.44	2.4
981022	991007	-0.12	1998.81	1999.77	0.96

2.4 Discussion of InSAR Results

The results of this and previous studies clearly indicate that detection of underground facilities using InSAR is possible under favorable circumstances. Ideally, these would include high phase correlation, as typical of urban or arid areas, and shallow tunnels excavated in soil or soft rock. An interesting aspect is time-dependent uplift that occurred after excavation of two of the Los Angeles segments and with other tunnels, which probably are caused by hydromechanical effects associated with excavation-induced groundwater pumping. This might also occur at hard rock sites.

Analysis of the InSAR results for the Los Angeles subway indicates that the application of a time series technique using multiple interferograms is essential to provide a clear spatial image with high signal-to-noise. Of the three techniques tested (stacking, SBAS, and PSInSAR), stacking and PSInSAR performed the best in this environment and with the available data set. Stacking has the advantage of simplicity and ease of automation, but has poor time resolution and requires an accurate DEM. PSInSAR resolved the signal spatially and temporally but requires more processing. The most effective strategy for analysis of similar datasets appears to be stacking followed by PSInSAR analysis, as this will provide redundant and robust results for both the spatial and temporal distribution of subsidence. SBAS would probably perform better if more interferograms were available to cover the time period of maximum excavation activity.

An area of future development would be to develop an automated method of detecting and evaluating the signals. One possible approach is matched filtering. Matched filters cross-correlate the image with a specified pattern, but require a pattern template. In

the Los Angeles case, the geometry of the Los Angeles subway is known and therefore could be used to provide the template, but for detection of clandestine facilities the pattern would not be known a priori. It is possible to use the stacked image as a template and by cross-correlating the template with the individual interferograms , an associated detection level can be obtained.

3. Inversion of Displacements to Characterize Subsurface Facilities

The surface displacement field resulting from an underground excavation is dependent upon the volume, shape and depth of the excavation and on the constitutive mechanical properties of the host rock or soil and overburden. The surface displacements are related to the characteristics of the source by a geomechanical model that incorporates the relevant source and constitutive parameters. Two general approaches can be employed to infer the characteristics of a subsurface deformation source from the pattern of surface displacements. The first is more or less trial and error forward modeling to find the source that reproduces the observed data as closely as possible, and the second is to incorporate the geomechanical model in a formal inversion of the data. Inversion is the most rigorous approach because it searches systematically through a large number of trial source models following a procedure that progressively assesses the fit of the data predicted by the source models to the observations to converge to some form of best-fit solution.

Conventional deterministic inversion approaches search for a single solution that provides the minimum misfit, together with estimates of the uncertainties (variance, covariance) on the parameters of that solution. However, these conventional methods can deal with only linear or, at best, weakly non-linear forward models, and are best suited to simple source geometries. Furthermore, they perform a localized rather than a global search and so can become trapped in a local minimum, rather than the global minimum corresponding to the true source. Stochastic inversion approaches, on the other hand, generally use some form of Monte Carlo technique to perform a global search of the model space by running forward simulations for a large number – typically thousands to tens of thousands - of trial source models to identify the set of models that are consistent with the observations and prior constraints.

3.1 Stochastic Inversion Approach

In this study we adapted LLNL's general-purpose stochastic inversion program, the "Stochastic Engine" (SE), to carry out inversions of surface displacements to characterize subsurface excavation geometries. The SE implements a Bayesian Markov Chain-Monte Carlo (MCMC) inversion procedure to perform a global search of the model space, and is described in Appendix A.

For the present application, trial source models generated within the base representation consist of one or more basic 3D void shapes (cylinders or rectangular parallelepipeds) combined in various arrangements and at varying locations to represent excavation geometries. The configuration of each proposed model is based on a set of intersecting lines, each representing the axis of one component, contained within a defined build volume. Perturbation transitions permitted by the base sampler are:

- Add or delete components, up to a defined maximum number
- Change the size of one or more components within defined bounds
- Change the depth of the entire facility
- Translate and rotate the entire facility in a horizontal plane, maintaining interconnections and keeping the locations of defined "outside" points (e.g. portals) fixed

The geomechanical forward models used in the stochastic inversion can be empirical, closed-form analytical elasticity solutions, or, possibly numerical, and are discussed in the Section 4 below.

We performed functional tests of the SE implementation based upon the layout and site material properties of the Heathrow Express trial tunnel (see Appendix B). Fixing the geometry and depth of the tunnel, we used the commercial finite element program COMSOL to synthesize the surface displacement field by varying the deformation of the tunnel walls until the synthetic data matched a measured vertical displacement profile perpendicular to the tunnel, as shown in Figure 11. We then inverted a set of regularly spaced east-west profiles through the synthetic data for the tunnel configuration and location. Peck's (1969) empirical 2D relationship (see Section 4.1) was used as the forward model in the SE. The S_{max} and i parameters (see Section 4.1) were determined by the relationships proposed by Ercelebi et al (2005) and Atkinson and Potts (1977), respectively.

The inversions ran four independent Markov chains, each having a different starting model, for 3,000 iterations per chain. Prior bounds on the tunnel length and diameter were 100m-700m and 5m-10m, respectively, but the depth was fixed. The tunnel was allowed to rotate through 360°. The convergence behavior of one of the chains during one inversion is plotted in Figure 12, which shows that the inversion behaved as expected in converging to a relatively narrow range of high likelihood models within relatively few iterations and after about 200 trials had been accepted. The orientations of all of the models within the high likelihood range determined by all of the chains are within a few degrees of the actual tunnel and their centers are within ±10 m of the actual location. The tunnel length varies is the most poorly constrained parameter, varying over approximately ±50m at each end. These tests demonstrated the basic functionality of the base representation and sampler and that the implementation is stable and well behaved.

4. Geomechanical Forward Models

In this section we discuss evaluation of geomechanical forward models as a basis for selecting those suitable for use in the stochastic inversion. The evaluation was based on a comprehensive review of available models and current techniques, and included empirical, analytical and numerical methods. All of these methods are currently used in geotechnical practice to evaluate the deformation and stability of excavations and to predict the occurrence of surface displacements that may pose a risk to existing structures. They are also used in the mining sector, but generally to a lesser degree of sophistication.

Linear elastic, time-independent deformation can be described for some source types and homogeneous or layered geologies by closed-form two- and three-dimensional analytical solutions, and are generally applicable to competent rock. In many cases they also provide an adequate description of the bulk deformation of some soils, even if

localized plastic deformation takes place in vicinity of the excavation itself. In other cases, numerical elastoplastic modeling may be needed to describe satisfactorily the behavior of loosely consolidated soils and highly jointed rock. A numerical method is also required to model the poroelastic response that occurs when the source excavation induces significant groundwater flow, resulting in time-dependent deformation that may continue over a considerable length of time following excavation activities. Empirical models can implicitly include any of these constitutive behaviors. Three-dimensional models that predict maps of surface displacement can potentially make maximum use of InSAR data. However, 2D models can be used to invert a series of two-dimensional displacement profiles over, for example, a long tunnel far enough away from the ends.

While virtually any kind of material constitutive model can be accommodated in the SE framework, candidate models must satisfy three criteria, in addition to providing an adequate description of the deformation process to enable calculation of surface displacements with sufficient accuracy. First, the modeling algorithm must be computationally efficient enough to render the large number of forward realizations required in each stochastic inversion feasible. Second, the model should be generally applicable to a range of rock and soil types, and third, the model should contain as few parameters as possible, since parameter values are often difficult to estimate, particularly in denied-access situations. The first criterion favors closed-form analytical linear elastic or empirical models over more computationally demanding numerical approaches. Empirical and analytical forms are also easier to implement in the SE framework. The second criterion favors general physics-based models, rather than empirical relationships developed for specific geological conditions. Below we discuss our evaluation of available analytical elastic and empirical models. Because we found that significant limitations are evident in existing models, we also describe the development of a new elastic formulation for a cylindrical tunnel, and discuss the feasibility of implementing an efficient numerical method.

4.1 Empirical Models

Empirical methods are the fastest and least complicated method of estimating surface deformation, and are widely used in geotechnical practice to predict 2D transverse, and sometimes longitudinal, surface displacement profiles above tunnel excavations. However, empirical relations generally have little or no theoretical basis and most contain no explicit dependence on material properties. Therefore, they are usually limited to a narrow range of soil or rock types and construction techniques similar to those used in the development and calibration of the relationship. Many of the empirical relationships assume incompressible behavior (i.e. the material undergoes no volume change). Typically, the parameters in the relationship are determined during the initial stages of an excavation, and then applied to subsequent stages. This approach, of course, is not applicable in denied-access areas.

The most commonly used empirical techniques are based on the relationship proposed by Peck (1969), in which the vertical displacement profile transverse to the axis of a circular tunnel excavated in soft ground and well behind the tunnel face is approximated by the Gaussian distribution function (Figure 13):

$$S(y) = S_{\max} \exp\left(\frac{-y^2}{2i^2}\right)$$

where S is the vertical subsidence at perpendicular distance y away from the tunnel axis, S_{max} is the maximum settlement at y=0, and i is the point of inflection of the curve. A plethora of different methods for estimating S_{max} and i have been published by various authors, most of which are specific to particular combinations of construction technique and geologic conditions. One example relationship for S_{max} that has an explicit dependence on the tunnel radius and depth and material properties was suggested by Ercelebi et al. (2005):

$$S_{\max} = 0.785\gamma Z_0 \frac{4R^2}{iE}$$

where R and Z_0 are the radius and depth to the tunnel, and E and γ the Young's modulus and specific weight (=ρg) of the medium. Examples of relationships for the inflexion point, i, given by (Atkinson and Potts, 1977) are:

$$i = 0.25(1.5Z_0 + 0.5R)$$

for dense sand or over-consolidated clays, or

$$i = 0.25(Z_0 + R)$$

for loose sand.
An alternative to Peck's relationship proposed by (Bucek, 2009) is:

$$S(y) = S_{\max}\left(1 - \frac{y}{L}\right)^4 \exp\left(\frac{4y}{L}\right)$$

where L is the half-length of the entire subsidence trough.

Under plane strain conditions for incompressible cohesive materials such as soft clays O'Reilly and New (1982) suggested that horizontal surface displacements can be described using:

$$H(y) = \frac{y}{Z_0} S(y)$$

where $S(y)$ is the vertical displacement given by Peck's relationship.

Empirical estimates of longitudinal displacement profiles (i.e. settlement in front of and behind the tunnel excavation face in the direction of excavation) have not been well studied. However, Attewell and Woodman (1982) and New and O'Reilly (1991) proposed longitudinal displacement profiles for incompressible materials in the form of cumulative distribution functions, based on Peck's (1969) Guassian model.

When considering multiple tunnels, the settlements at the surface calculated for each tunnel separately can be superimposed to obtain an estimate of the deformation due to both tunnels provided that the tunnels are not closer than one tunnel diameter to each other (Mair et al., 1996). For example, New and O'Reilly (1991) proposed the following

relationship for twin tunnels of the same size and at the same depth with axial separation *A:*

$$S(y) = S_{\max}\left[\exp\left(\frac{-y^2}{2i^2}\right) + \exp\left(\frac{(-y+A)^2}{2i^2}\right)\right],$$

4.2 Analytical Linear Elastic Models

Analytical methods employ closed-form solutions that can account for different medium properties and, to some extent, different excavation configurations and deformation modes. Therefore, they can be applied to a wide range of geological materials as long as the constitutive behavior can be described, at least approximately, as elastic and the constitutive parameters can be estimated. Analytical elastic models are available only for simplified homogeneous elastic half-spaces or horizontal layering. While this appropriate for many geological environments, it limits modeling accuracy in situations when there is significant 3D heterogeneity. Semi-empirical modifications to the solutions can also take into consideration specific aspects of the method of excavation (e.g. Loganathan and Poulos, 1998).

The basic modes of deformation of a circular tunnel excavated in a medium pre-stressed under gravity are shown in Figure 14. The first component, referred to as "ground loss" in the geotechnical literature, is the ratio of the radial convergence that the tunnel would experience under isotropic (hydrostatic) gravitational loading to the final tunnel radius (i.e. the radial strain). The second, referred to as "ovalization", conserves void volume and occurs when the vertical, σ_v, and horizontal, σ_h, stresses are unequal, i.e. when the coefficient of later resistance, K_0, is less than one in $\sigma_h = K_0\sigma_v$, or possibly due to the proximity of the ground surface to shallow excavations. The third component is rigid-body upward displacement of the entire excavation due to buoyancy when the weight of the tunnel (which may be lined) is less than the weight of the excavated material.

Linear elasticity theory has been applied to underground excavation problems since Mindlin (1940) developed an exact 3D solution for the stresses surrounding a circular tunnel in a linear elastic half-space subject to gravitational loading. However, the problem of deriving displacements within and at the surface of the half-space, which are not included in Mindlin's solution, has proved to be challenging, and has been the subject of considerable renewed study over the past 15-20 years.

Pender (1980) developed exact point-source solutions for the stresses and displacements surrounding a tunnel in a pre-stressed infinite whole-space, but these cannot be used directly to calculate surface displacements. Sagesta (1987) developed an exact 3D point source solution for the displacements in an incompressible half-space resulting from radial contraction *prescribed* at the tunnel wall. The assumption of incompressibility is quite restrictive, but may, for example, be applicable to the undrained deformation response of soft clays.

Verruijt and Booker (1996) extended Sagesta's solution to include prescribed radial contraction and ovalization of the wall of a tunnel in an elastic medium to derive approximate solutions for stresses and displacements under the assumptions of (2D)

plane strain [an error in the ovalization term in this relationship was corrected by Strack and Verruijt (2000)]. We also derived an exactly equivalent plane strain solution from the 3D dislocation Green's functions for a point deflation source developed by Okada (1992). Similarly, Wang et al. (2008) present Green's functions for dislocations in a flat-layered viscoelastic half-space. Verruijt and Booker and Okada employed singular solutions for a point source in an infinite plane and infinite half-space, respectively. As discussed in Appendix C, introducing the free surface requires a virtual image source above it to balance the point source within the medium in order to satisfy the zero-stress boundary conditions on the surface. Such solutions are approximate because the influence of the image source on the deformation at the tunnel walls is neglected. These solutions are adequate for excavations deeper than about 1½ tunnel radii (see Mindlin, 1940).

The prescribed deformation of the tunnel wall in these approximate solutions (and also in the exact solutions discussed below) is given as the ratio of radial displacement to the final tunnel radius. Therefore in an application like ours, where the tunnel radius is an unknown to be determined by inversion, there is a tradeoff between it and wall displacement; in other words, we can determine the strength of the source expressed (in 2D) as the change in tunnel cross-sectional area. This tradeoff does not exist when the problem is posed as one of introducing an excavation of given dimensions into a medium pre-stressed under gravity, when the wall deformations take place naturally.

Verruijt (1997) employed conformal mapping and the complex variable method of Muskhelishvili (1953) to derive exact 2D plane strain solutions for the stresses and displacements caused by prescribed displacements of the tunnel walls. He noted that in order for the calculated displacements to go to zero at infinity, the tunnel must undergo a downward rigid body displacement. However, subsequent work by Verruijt and Booker (2000) and Strack (2002) to derive exact solutions for a circular hole of given radius introduced into a half-plane under gravitational pre-stress highlighted the important influence buoyancy - neglected in previous solutions – has on surface displacements. The buoyancy force resulting from removal of material causes an *upward* rigid body displacement of the tunnel. This produces heave (upward displacement) at the surface, which results in subsidence troughs that are shallower and up to 50% narrower than those predicted by approximate and exact elastic solutions that neglect the buoyancy force (Verruijt and Strack, 2008; Klaar, 2006), and appear to be in better agreement with measured displacements (see Figure 15).

Unfortunately, the exact 2D displacement solution contains a logarithmic singularity that results in calculated displacements that are arbitrary to within a constant rigid body displacement, although the stresses and strains are uniquely determined (Strack and Verruijt, 2002; Verruijt and Strack, 2008). Strack and Verruijt point out that this unphysical behavior is a characteristic of all exact plane strain solutions. They suggest that it can be mitigated in the vicinity of the tunnel by requiring the displacement to be zero at an adequate distance from the source, but observe that the choice of the point of constraint has a large effect on the calculated surface heave. Klaar (2006) and our own work also show that surface displacements calculated by 2D finite difference and finite element models are dependent to some degree on the depth of the assumed rigid lower boundary of the model.

4.3 Comparison of Models with Measured Data

We evaluated empirical models and the approximate 2D elastic model derived using Okada (1992) dislocation solutions (i.e. no buoyancy) by comparing surface vertical displacement profiels with available data from the case histories detailed in Appendix B, which summarizes tunneling projects for which both surface deformation and detailed engineering and material property data are available. We also used finite element modeling to benchmark some of the models. Results from the exact 2D solutions of Verruijt and Booker (2000) and Strack and Verruijt (2002) computed using the codes MINDLIN and CircularTunnel supplied by A. Verruijt at http://geo.verruijt.net are not very informative because of the sensitivity of the surface heave to the assumed point of zero-displacement, so are not discussed.

Figure 15 shows example comparisons of vertical displacement profiles, the first transverse to the axis of the Heathrow Express trial tunnel and the second to the St. James Park underground extension (see Appendix B). The figures show results from the approximate elastic solution and two different empirical models. The models for each tunnel used the material parameters given in Appendix B. The approximate elastic model is applicable, as in both cases the tunnel depth is significantly greater than its diameter. This also enabled us to use Pender's (1980) solution to calculate tunnel convergence, which then was used as input to the dislocation model. It can be seen that in both cases the elastic model predicts deeper and much broader subsidence troughs than observed, consistent with the lack of a buoyancy component, although the subsidence amplitude is close to the observations at St James Park.

All of the empirical models use Peck's (1969) Gaussian form. S_{max} is given by the relationship of O'Reilly and New (1982) in Models 1 (Heathrow) and 4 (St. James Park), and by Ercelebi et al. (2005) for Models 2 and 5. The i parameter is taken from Ercelebi et al (2005) for Models 1 and 5, O'Reilly and New (1982) for Model 2, and Clough and Schmidt for Model 4. The results show that unless an empirical relationship has been specifically calibrated and shown to be appropriate for a particular site, a large range of behavior can be predicted, depending on the form of the selected relationship. Obviously calibration and validation would not be possible for a denied-access site. The profile calculated by the finite element method shows that very good agreement with data can be achieved if the relevant material properties can be closely estimated.

The conclusion drawn from the comparisons we carried out and from the discussions above is that none of the empirical or analytical models that are presently available are truly adequate for use in stochastic inversions to characterize underground facilities. We addressed this in two ways: First we developed a new 3D analytical solution for a cylindrical tunnel in an homogeneous elastic half-space that includes buoyancy, and second we began a detailed assessment of the feasibility of using a highly scalable and hence fast finite element approach.

4.4 Effect of Cavity Shape

Excavations can have a variety of shapes, including circular, rectangular and more complex curvilinear (horseshoe) cross-sections. However, the analytical and empirical solutions discusses above have been derived for subsurface openings having circular or equivalent circular cross sections. We investigated the effect of tunnel shape on surface vertical displacements by carrying out 2D finite element modeling of the displacements produced by four representative void shapes having approximately equal cross-sectional

areas. The resulting displacement profiles are compared in Figure 16. The largest difference in maximum surface subsidence - between the circular and approximately square cross sections - is about 15%. The displacement profiles for the horseshoe and the other compound cross-section shown lie between these two extremes.

4.5 3D Solution for a Cylindrical Tunnel in an Elastic Half-space

Verruijt and Strack (2008) suggest that the unphysical displacements inherent in exact plane strain analytical solutions probably results from unmodeled 3D effects. Our review of the current state-of-the art revealed no 3D solutions for elastic deformations that arise from excavation of tunnel- or mine-like cavities in media having a free surface. In addition to point spherical dilation sources, some approximate (e.g. Sun, 1969; Davis, 1986) and exact (e.g. Fialko et al., 2001) solutions exist for particular configurations of pressurized ellipsoidal crack-like voids in a 3D elastic half-space, but the crack geometries are not directly applicable to tunnel-like voids and these solutions do not consider buoyancy. It may be possible to construct an appropriate 3D dislocation solution from the Okada (1992) Green's functions, but that would not include buoyancy either and would not resolve the tradeoff between the tunnel dimension and wall displacement.

We therefore decided to develop a new 3D solution, beginning with a cylindrical tunnel embedded in an homogeneous elastic half-space under gravitational loading. The derivation of the solution based on the harmonic potential method of Papkovitch and Neuber (see Sokolnikoff, 1956, pp. 328-335) is discussed in Appendix C. The resulting compact expressions for surface displacements includes an uplift term due to the buoyancy of the tunnel. Although, as discussed later, predicated long-wave uplifts appear to be excessive, indicating that the solution is still not entirely complete, it predicts relative downward displacements above the excavation that are in generally good agreement with observed subsidence troughs.

4.5.1 Comparison of the 3D Elastic Solution with Measured Data: Figures 17 and 18 compare vertical displacements calculated using the 3D solution with the measured profiles over the Heinenrood Tunnel in the Netherlands and the Heathrow Express trial tunnel, using the geological material parameters detailed in Appendix B. The geological structures at these sites are relatively uniform. The measurements in each case extend only as far as the edges of the subsidence troughs, which presumably are approximately coincident with the locations of the maximum uplift produced by the tunnel buoyancy. Therefore, the model displacements in the figures are shown relative to the maximum calculated uplift.

Figure 17 shows that the calculated relative displacements within the central subsidence trough are in remarkably good agreement with the measurements over the Heinenrood tunnel. The pronounced "tails" of the model profile result from the buoyant response upon which the subsidence is superimposed. The longer wave buoyant term has a logarithmic dependence on the tunnel length (Eq. 22, Appendix C), and the large uplift predicted for this long (~1 km) tunnel is counter intuitive and unlikely to be observed in practice (see Section 4.5.2 below).

The Heathrow tunnel was excavated in London clay. The K_0 value for the Heathrow site is not given in the references, but we adopted a value of 0.8, which is within the range typical of London clay at the St. James Park site (Appendix B). Figure

18 shows that the subsidence calculated using this K_0 value is in good agreement with observations along two of the measured profiles, although the uplift at the edge of the central subsidence trough is again somewhat overpredicted.

4.5.2 Discussion of the Large Heave Peak: Our new 3D elastic solution predicts relative surface displacement profile shapes across tunnels that appear to agree with actual observations. However, this relative subsidence sits atop a potentially greater uplift caused by the tunnel's buoyancy. Such a large heave is counter-intuitive, and probably not observed in practice. The heave represents an increase in gravitational potential energy of the surface material, whereas we know that hollow objects are buoyed upwards because this decreases the potential energy.

We believe that such a gravitational effect can be accommodated consistently in our model by including an additional basis function for the harmonic potentials that are used in the Papkovitch-Neuber scheme to generate stresses and displacements (Ψ_{-1} in the notation of Appendix C). We did not include this term in our scheme initially because it diverges far from the tunnel and because the boundary conditions can be satisfied without it. In retrospect, neither of these reasons appears valid, and in fact Ψ_{-1} is associated with buoyancy. With the extra degree of freedom given by this term, the gravitational potential energy associated with the perturbation can be adjusted: it must be null for global equilibrium. As a consequence, the average vertical displacement over the surface area will be zero, and this will reduce the upward displacement in the current solution.

Strack (2002), in his treatment of the 2D tunnel problem, assigns a separate center to each term in the potential expansion, not necessarily coincident with the physical center of the tunnel. We must either verify that this does not introduce additional freedom in our potential expansion at first order, or else properly account for the gravitational effects of this freedom.

Finally, the assumption that the background stress profile will cancel the weight of a displaced volume is not strictly true. The weight of the element can be shown to vary with its displacement, again from consideration of the gravitational potential, and the resulting mismatch in stress acts as a restoring force. This, however, is a second-order effect.

4.6 Feasibility Assessment of Finite Element Modeling within the SE

Numerical forward modeling techniques, such finite element (FE), finite difference (FD) and boundary element (BE) methods, hold several large advantages over analytical approaches. These include first of all the ability to model deformation in two- and three-dimensional geological structures, and to handle arbitrary cavity geometries and relatively complex, compound configurations. The other great advantage of FE and FD methods is that they provide the flexibility to model a wide range of constitutive behaviors, including non-elastic behavior such as elasto-plastic deformation and time-dependent behaviors such as creep and poroelasticity. These methods therefore hold the potential to improve significantly the accuracy of predictions of surface displacements over the wide range of shallow geological environments likely to be encountered.

Given the significant limitations of existing empirical and analytical elastic modeling approaches, this flexibility is very appealing. However, coupling the power of numerical modeling to the SE comes at the cost of additional challenges. The first is simply the computational resources and time required to run FE or FD models involving large grids many thousands of times; the conventional BE method is substantially better

in this respect, since meshing of only the cavity walls is required, but it lacks the ability to deal with non-elastic materials. The second challenge is that automatic mesh generation is required for every realization of the facility configuration proposed by the SE sampler. We therefore decided to examine these challenges to evaluate the feasibility of utilizing an advanced FE method in the stochastic inversion.

GEOCENTRIC is a highly scalable parallel FE code for modeling geologic systems, developed by Josh White (White and Borja, 2008, 2011). It contains solvers for elastic, elastoplastic, and coupled poromechanics problems, and has been written to take full advantage of high-performance computing platforms. This is accomplished in GEOCENTRIC by employing efficient algebraic multigrid preconditioning techniques to accelerate the convergence of the solvers. Figure 19 illustrates the parallel performance of the code when used to solve a poroelastic problem on grids of various sizes. Figures 19a and b plot the number of iterations needed for convergence against the number of degrees of freedom in the problem and the corresponding wall-clock time, respectively, against the number of cpus used. Excellent scalability is demonstrated by the fact that both the number of iterations and the clock time remain almost constant across the range of degrees of freedom in the system.

Automated mesh generation is accomplished using the code CUBIT (http://cubit.sandia.gov). We found that CUBIT can generate high-quality meshes for tunnel realizations such as those shown in Figure 20 typically in just a few seconds, which is certainly within the range of per-realization clock times required for viable implementation in the SE. Using CUBIT, we have developed a fully automated script that generates each mesh realization given several input parameters describing the tunnel geometry.

To date, an interface between the SE and GEOCENTRIC has been written, so that GEOCENTRIC may be run dynamically from within the SE. The initial testing of this interface has been applied to a related project, in which the SE calls GEOCENTRIC as the forward model to invert for the pressure plume location in a carbon sequestration reservoir, given InSAR measured surface displacements. With relatively little modification, we believe this same interface can be used for tunnel inversions as well.

5. Conclusions

Repeat-pass synthetic aperture radar interferometry (InSAR) is now a well-established technique for mapping small millimeter- to centimeter-scale displacements on the Earth's surface at regional to local scales. In this report we have discussed the development of a methodology to exploit ground surface displacement maps produced from commercially available satellite synthetic aperture radar (SAR) data to detect and characterize subsurface facilities. The method development involved three elements: (1) Evaluation of the ability of InSAR to detect and measure surface displacements from underground excavations; (2) adaptation of a stochastic inversion procedure to invert the displacement data to characterize the depths, shapes and sizes of the underground facilities; and (3) evaluation of geomechanical forward models to select those suitable for use in the stochastic inversion.

In the first element we demonstrated the potential of InSAR by imaging surface displacements associated with the excavation of sections of the Los Angeles Metro system. Despite large displacements fluctuations over short distances seen on ground-based measurements, displacement signals that trace the course of the excavations are

clearly seen even on single-pair interferograms, and become more distinct by stacking multiple interferograms and by permanent scatterer time series processing (PSInSAR). Stacking is the most basic means of increasing the signal-to-noise ratio, and we expect significant improvement by further permanent scatter analysis. Combining PSInSAR with a short-baseline subset method could substantially improve InSAR accuracy and resolution for locations where sufficient numbers of interferograms are available.

We completed adaptation of LLNL's general-purpose Markov Chain-Monte Carlo stochastic inversion framework, the "Stochastic Engine" (SE), by developing and implementing a module to represent and sample sequential realizations of excavation configurations that are used as trial deformation sources in the inversion. This representation/sampler can propose complex configurations consisting of interconnected basic void shapes, perturbing the configuration from iteration to iteration following a Markovian rule. The SE implementation performed satisfactorily in preliminary functional tests employing a simple empirical forward model, and is ready for use. Further tests will be needed to ensure functionality when more sophisticated forward models are interfaced to the SE core. Two features favor this kind of stochastic inversion approach for this application: The first is its ability to deal with relatively complex deformation sources and forward models; and the second is that the inverse solution is a posterior probability function over alternative models that can be input to risk-based decision analyses to evaluate subsequent strategies.

The third element turned out to claim more of the effort in the study than originally anticipated. At the outset of the project we expected that the types of models that would be computationally fast enough to render feasible the large numbers of forward calculations required in each inversion would be closed-form empirical and analytical models, rather than numerical models. However, during the comprehensive review of existing models and modeling approaches conducted as the first task of the project, we found that, in general, each of the empirical models used in geotechnical practice is limited to specific narrow ranges of soil and rock types, and typically the model parameters are calibrated by initial in situ testing at each site where the model is applied. This clearly limits the portability of the relationships, particularly to denied-access areas. Analytical elastic solutions, on the other hand, rely on just a few generic parameters that may be relatively easy to estimate for a site within realistically narrow bounds, and are therefore portable. However, older displacement solutions do not consider the important contribution of buoyancy to surface displacements cause by excavation of a void. More recent 2D solutions do include buoyancy, but the displacements are determined only to within an arbitrary constant.

We addressed these issues in two ways. The first was to develop a new 3D analytical elasticity solution that includes buoyancy for a cylindrical tunnel excavated in an elastic half-space. The new solution calculates relative displacement profiles above two tests tunnels that provide good matches to ground-based measurements. However, the buoyancy term in the solution is dependent on tunnel length, and predicts long-wavelength surface uplift that is in excess of what would be expected, and probably measured. We believe that we understand the reason for this unphysical aspect of the solution, and continue to work on improving it.

The second approach we have taken is to reconsider numerical modeling with the SE procedure. This would allow much more flexibility in the types of forward models we could use, including elastoplasticity and time-dependent poroelasticity, and potentially in the complexity of the excavation configurations. The results of initial

feasibility tests using the parallel finite element code GEOCENTRIC together with the CUBIT code to generate meshes are encouraging. Automatic mesh generation for each realization takes only a few seconds, and GEOCENTRIC is a highly scalable code designed to take maximum advantage of available high-performance computing facilities. The next step will be to adapt the interface between SE and GEOCENTRIC already built for a related problem to the SE implementation for underground facilities.

References

Atkinson,J.H. , and D.M. Potts, Subsidence above shallow tunnels in soft ground, *Jnl. Geotech. Eng. Div., ASCE*, **GT4,** 307-325, 1977.

Attewell, P. B., and J. P. Woodman, Predicting the dynamics of ground settlements and its derivatives caused by tunnelling in soil, *Ground Engineering*, **15**, 13–22, 1982.

Berardino, P., *G.* Fornaro, R. Lanari, and E. Sansosti, A new algorithm for surface deformation monitoring based on small baseline differential SAR interferograms, *IEEE Trans. Geosci. Remote Sensing*, **40**, 2375-2383, 2002.

Bucek, R. (2009). Assessment of risk of building damage due to tunnelling, www.groundloss.com

Buckley, S. M., P. Vincent, and D. Yang, New ground truth ability from InSAR time series analysis, *Proceedings, 27th Seismic Research Review: Ground-Based Nuclear Explosion Monitoring Technologies*, 898-906, 2005.

Clough, W., and B. Schmidt, Design and performance of excavations and tunnels in soft clay, *Soft Clay Engineering*, Elsevier, Amsterdam, 1981.

Curlander, J.C., and R.N., McDonough, *Synthetic Aperture Radar: Systems & Signal Processing*, John Wiley & Sons, New York, 647 p, 1991.

Ercelebi, S., H. Copur, N. Bilgin, and C. Feridunoglu, Surface settlement predictions for Istanbul Metro tunnels via 3D FE and empirical methods, in *Underground Space Use: Analysis of the Past and Lessons for the Future,* Erdem & Solak (eds), Taylor & Francis Group, London, 163-169, 2005.

Ferretti, A., Prati, C. and Rocca, F., Nonlinear subsidence rate estimation using permanent scatterers in differential SAR interferometry, *IEEE Trans. Geosci. Remote Sensing*, **38**, 2202-2212, 2000.

Ferretti, A., A. Fumagalli, F. Novali, C. Prati, F. Rocca, and A. Rucci, A new algorithm for processing interferometric data-stacks: SqueeSAR, *IEEE Trans. Geosci. Remote Sensing*, **49**, 3460-3470, 2011.

Foxall, W., J. Sweeney, and W. Walter, Identification of mine collapses, explosions and earthquakes using InSAR: A preliminary investigation, *Proc. 20th Seismic Research*

Symposium, Santa Fe, NM, 1-9, 1998.

Loganathan, N., and H. G. Poulos, Analytical prediction for tunneling-induced ground movements in clays, *J. Geotech. Geoenv. Eng.*, 124(9), 846-856, 1998.

Mair, R. J., R. N. Taylor, and J. B. Burland, Prediction of ground movements and assessment of risk of building damage due to bored tunnelling, *in* R. J. Mair and R. N. Taylor (eds.), *Geotechnical Aspects of Underground Construction in Soft Ground*, Balkema, Rotterdam, 713-718, 1996.

New, B. M., and M. P. O'Reilly, Tunneling-induced ground movements: predicting their magnitude and effects. *Proc. 4th Int. Conf. On Ground Movements and Structures*, Cardiff, Pentech Press, **1**, 671-697, 1991.

O'Reilly, M. P., and B. M. New, Settling above tunnels in the United Kingdom—their magnitude and prediction, *Proc. Int. Symp. Tunnelling '82*, IMM, London, 173-181, 1982.

Peck, R. B., Deep excavations and tunneling in soft ground, *Proc., 7th Int. Conf. Soil Mech.* Mexico City, State of the Art Volume, 225-290, 1969.

Perski, Z., Applicability of ERS-1 and ERS-2 InSAR for land subsidence monitoring in the Silesian coal mining region, Poland, *Int. Arch. Photogrammetry Remote Sensing*, **32**, 555-558, 1998.

Sagaseta, C. (1987). Analysis of undrained soil deformation due to ground loss, *Géotechnique*, **37**, 301-320, 1987.

Scharroo, R., P. Visser, and G. J. Mets, Precise orbit determination and gravity field improvement for the ERS satellites, *J. Geophys. Res*., **103**, 8113-8127, 1998.

Sokolnikoff, I.S., *Mathematical Theory of Elasticity*, McGraw Hill, 1956.

Stirbys, A., F. Radwanski, R. Proctor, and R. Escandon, Los Angeles metro rail project – geologic and geotechnical design and construction constraints, *Engineering Geology*, **51**, 203-224, 1999.

Strack, O.E., Analytic solutions of elastic tunneling problems. Ph.D. Thesis, Delft University of Technology. Delft University Press, 2002.

Strack, O. E., and A. Verruijt, A complex variable soution for the ovalization of a circular tunnel in an elastic half plane, *Proc. Int. Conf. Geoeng 2000*, Melbourne, Australia, 2000.

Verruijt, A., A complex variable solution for a deforming circular tunnel in an elastic half-plane, *Int. J. Numer. Anal. Meth. Geomech.*, **21**, 77-89, 1997.

Verruijt, A. and J. R. Booker, Surface settlements due to deformation of a tunnel in an elastic half plane. *Géotechnique,* **46**, 753–756, 1996.

Wang, R., F. Lorenzo-Martin, and F. Roth, PSGRN/PSCMP—a new code for calculating co- and post-seismic deformation, geoid and gravity changes based on the viscoelastic-gravitational dislocation theory, *Computers & Geosciences*, **32**, 527–541, 2006.

White, J.A., and R.I. Borja, Block-preconditioned Newton-Krylov solvers for fullycoupled flow and geomechanics, *Comput. Geosci.*, **15**, 647-659, 2011

White, J.A., and R.I. Borja, Stabilized low-order finite elements for coupled solid-deformation/fluid-diffusion and their application to fault-zone transients, *Comp. Meth. Appl. Mech. Eng*., **197**, 4353-4366, 2008.

FIGURES

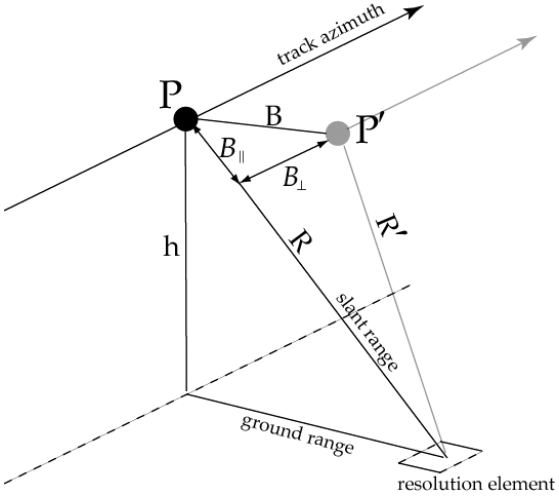

Figure 1: InSAR imaging geometry. P and P' are the positions of the satellite during two different orbits separated by baseline B.

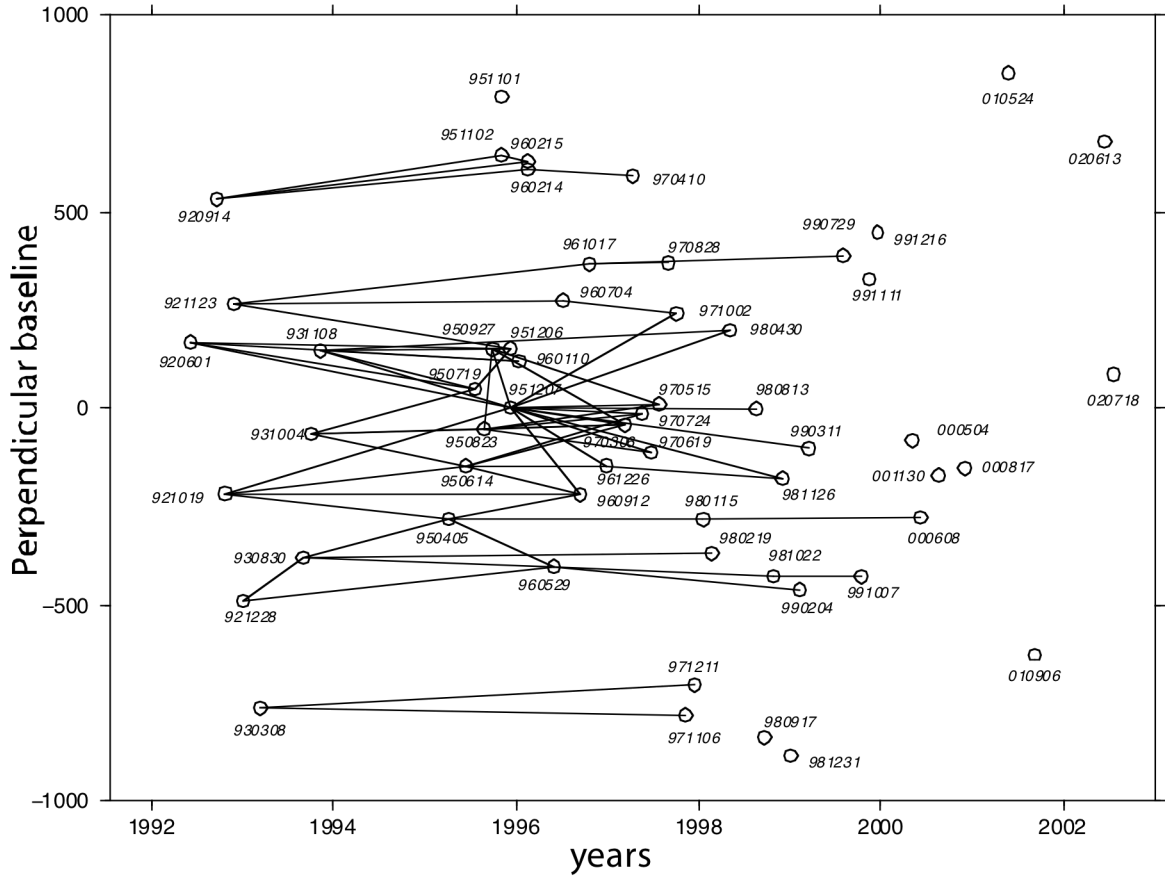

Figure 2: Baseline plot showing available data and interferometric pairs generated for analysis. Circles indicate each acquisition and lines connect pairs. The vertical axis is the distance between the satellites measured perpendicular to the surface of the earth. In general, interferogram quality is inversely proportional to both temporal baseline and perpendicular baseline.

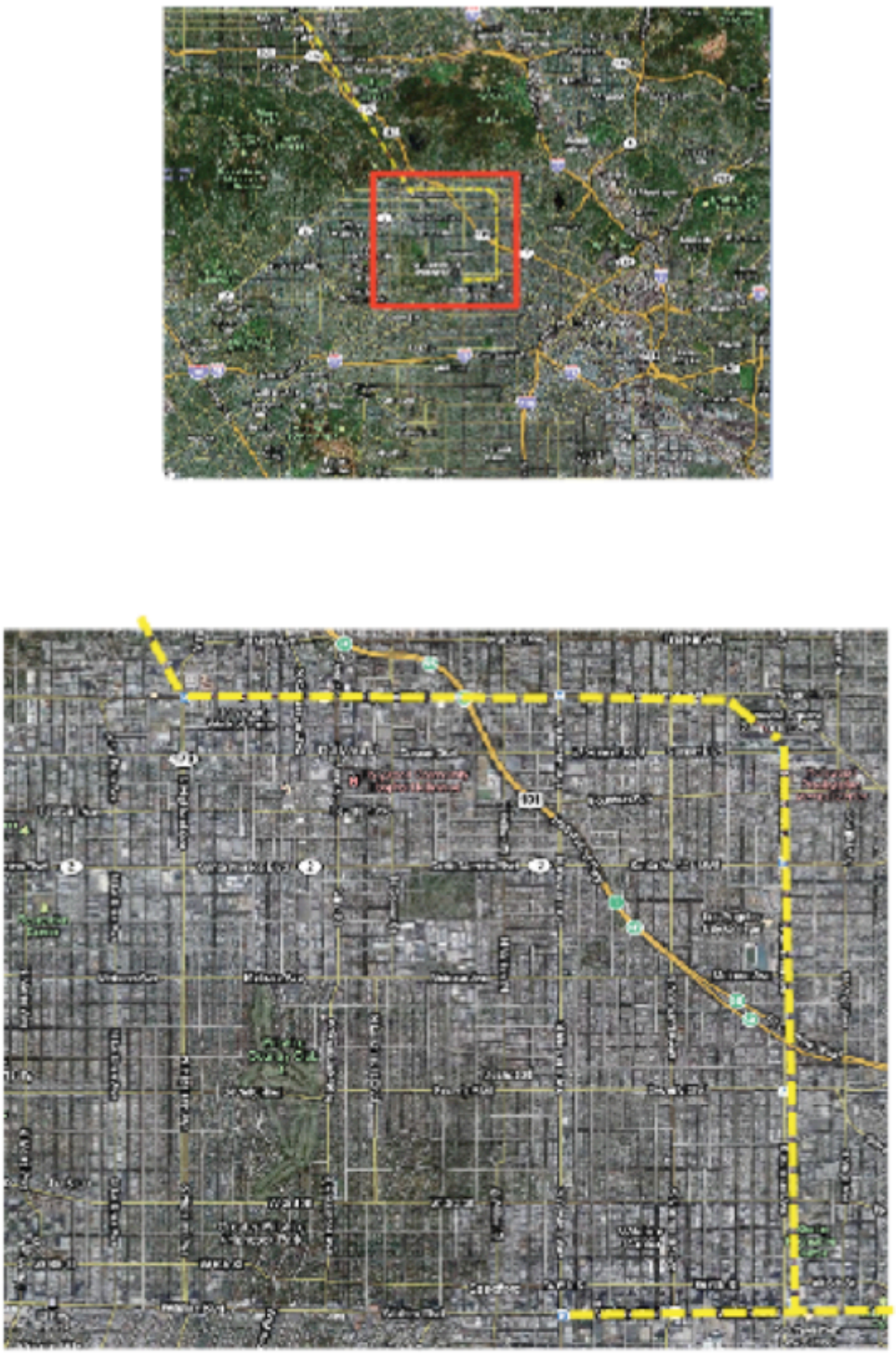

Figure 3: Optical image (*top*) of the Los Angeles region. Red square shows area of interest and yellow dashed line is the approximate path of the Red Line subway. Santa Monica mountains are the green area at the upper left and center above the red box. Larger scale image (*bottom*) with Hollywood Boulevard at the top.

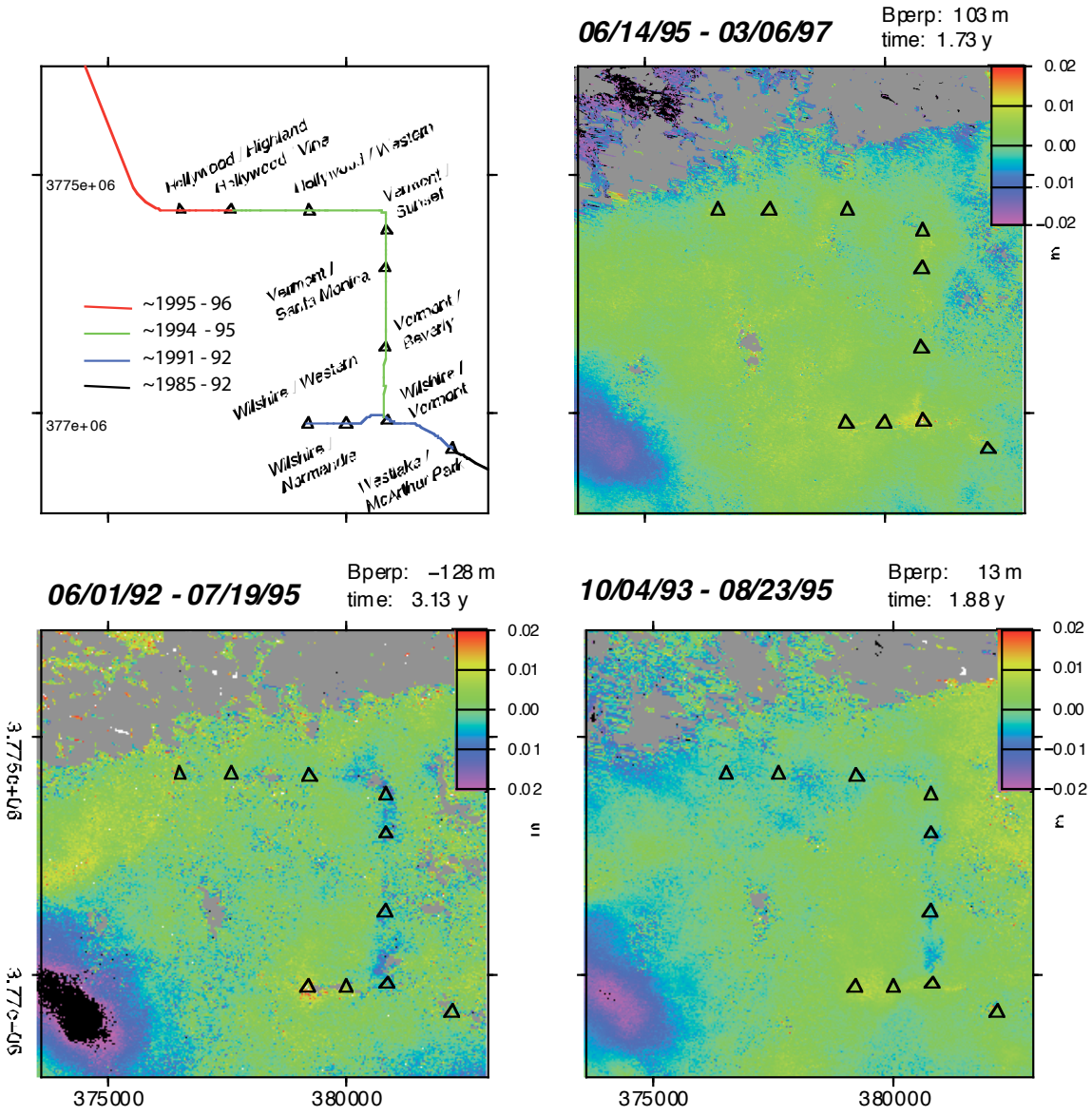

Figure 4: Three independent interferograms over different time periods. Low-coherence (< 18 %) pixels are masked out. A signal representing subsidence along the tunnel path is evident on the bottom two interferograms, which span the tunnel construction period. The upper right interferogram covers a time period after the tunnel construction and no signal is apparent.

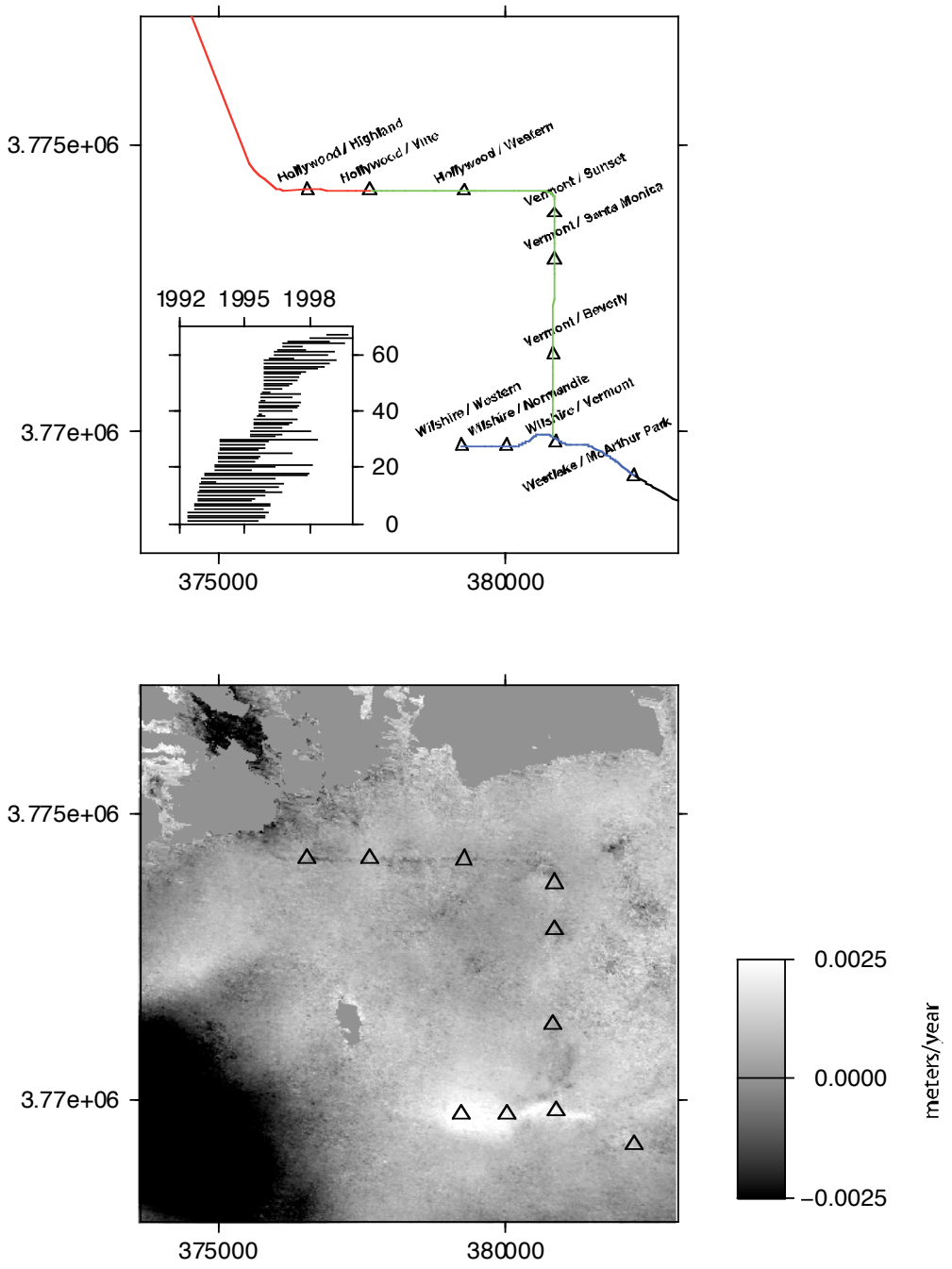

Figure 5: Map (*top*) of subway lines and stations. Insert shows time span of individual interferograms arranged in order from start date. Stack (*bottom*) of all interferograms divided by cumulative time per pixel to yield displacement rate per year. P ixels that are coherent in less than 50% of the interferograms are masked out. Triangles represent metro stations.

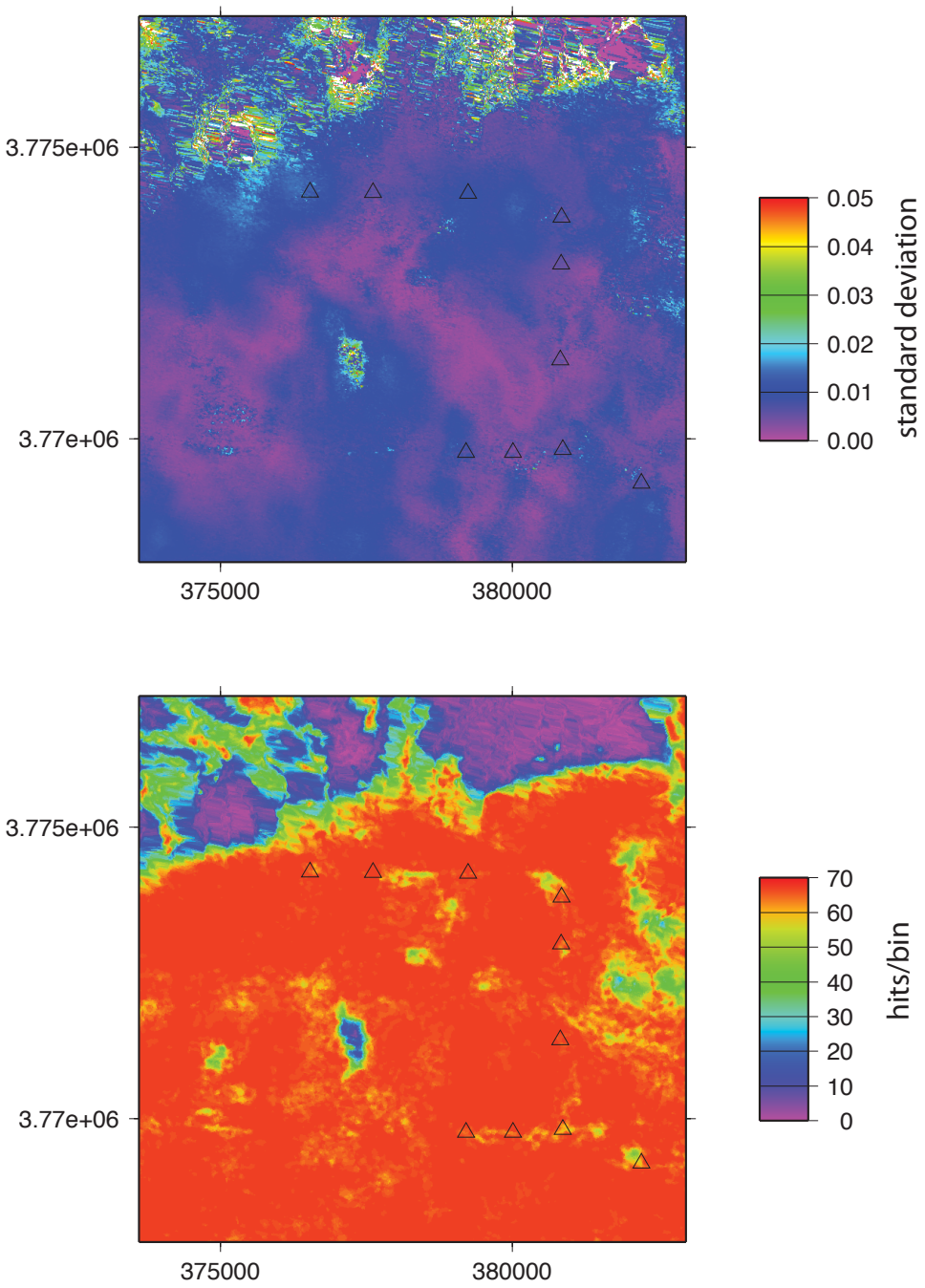

Figure 6: Pixel standard deviation (*top*) , and hits per bin (*bottom*) for the interferogram stack.

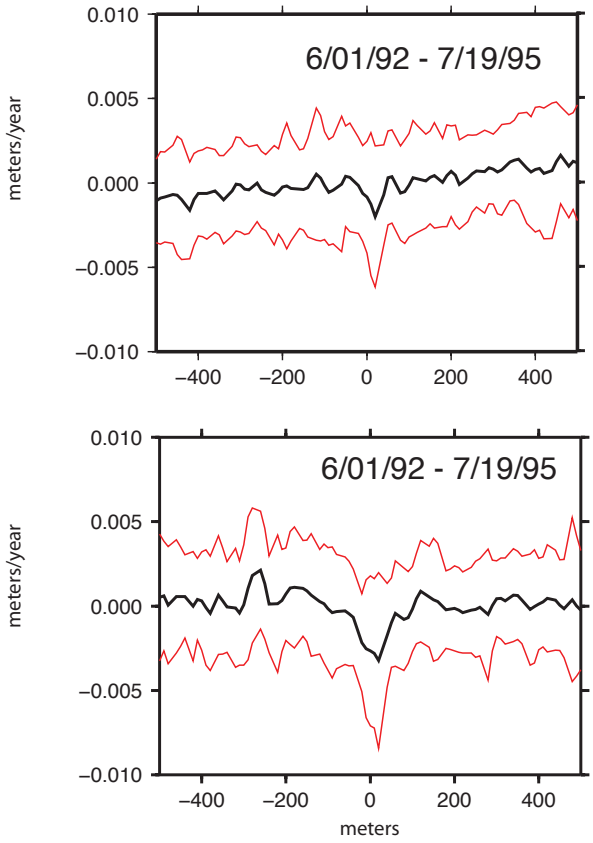

Figure 7: Profiles through the interferogram stack perpendicular to the Hollywood Boulevard segment between Highland Station and Edgemont (east of Western Station) at the mid point of the segment. Black and red lines are the mean and ±1 standard deviation of data averaged parallel to the subway.

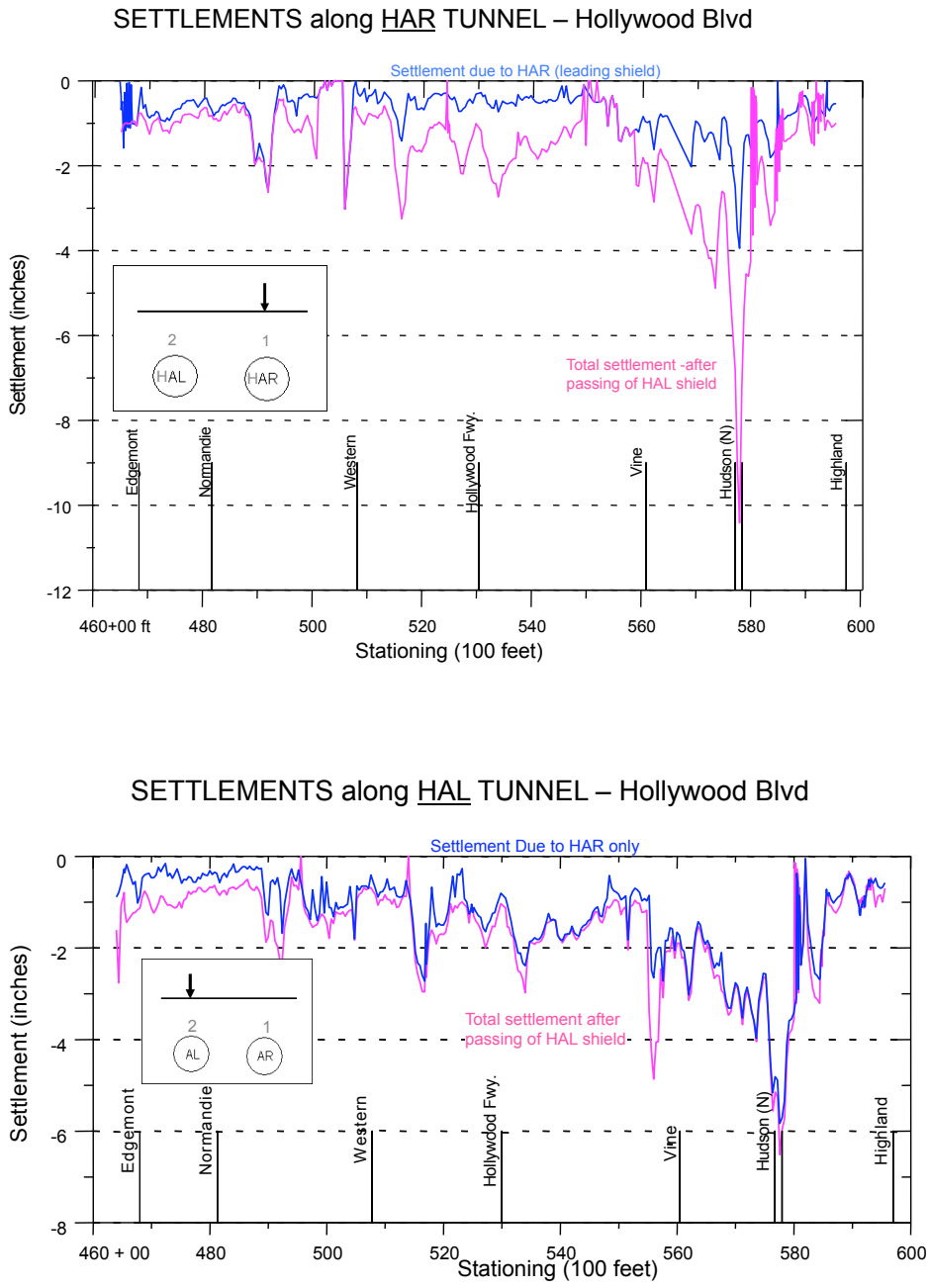

Figure 8: Ground-based measurements of subsidence made along the two tunnel axes as the tunnels were being excavated. Stations and intersections are marked at the bottom of each profile. Note that west is on the right (opposite of previous profiles). HAL and HAR refer to Hollywood left and right tunnels facing to the west in the direction of tunneling. (Courtesy of URS Corp.)

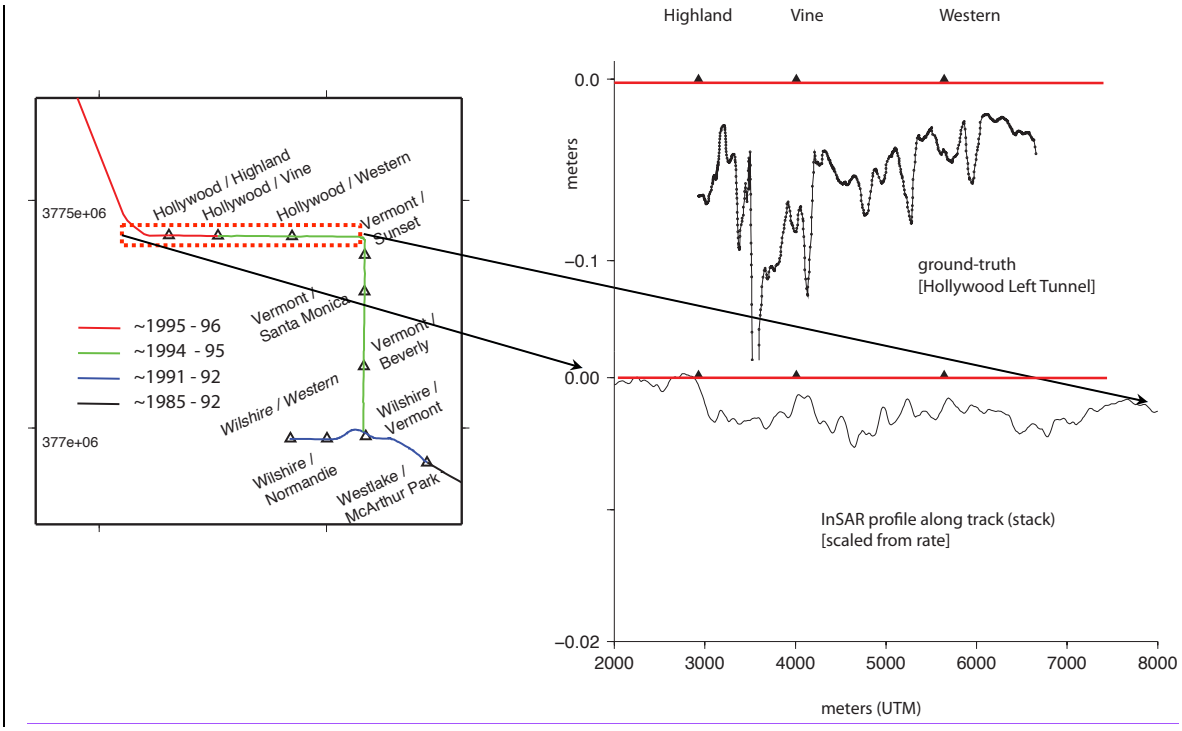

Figure 9: Profiles of displacement along the subway tunnel measured from InSAR compared to ground truth. Note the strong spatial variability in subsidence measured on the ground. The variability is also evident on the InSAR signal but is smoothed.

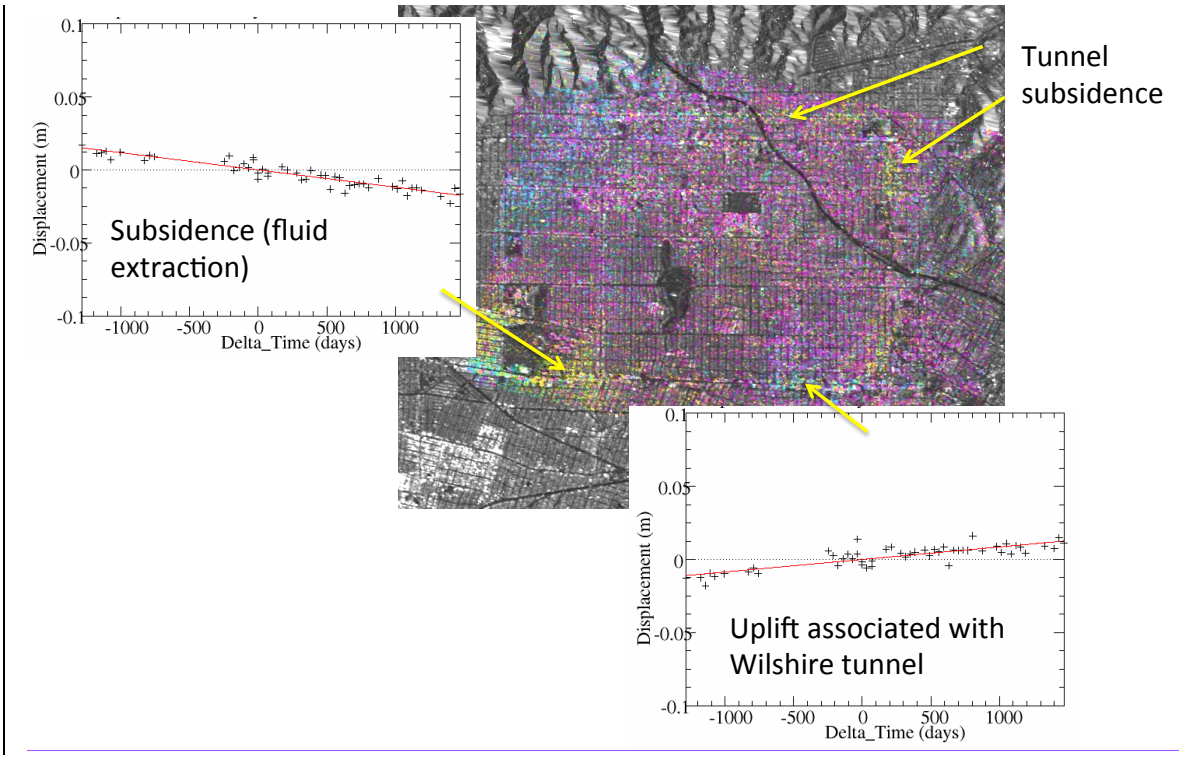

Figure 10. Permanent scatter analysis using a linear regression of deformation and corrections for atmospheric, baseline, and topographic effects. The permanent scatterers are superimposed on the radar amplitude image. Areas of subsidence and uplift are shown as yellow and blue, respectively. The inset on the *left* shows the displacement time series for a single pixel above an oil field where fluid extraction causes subsidence. The inset on the *right* shows the uplift above the Wilshire tunnel.

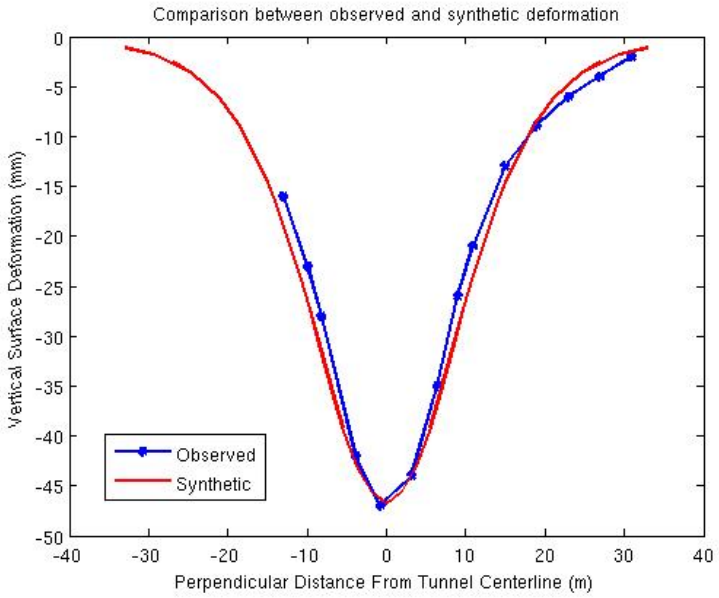

Figure 11: Comparison of measured data with a profile through a synthetic displacement field generated to test the Stochastic Engine implementation.

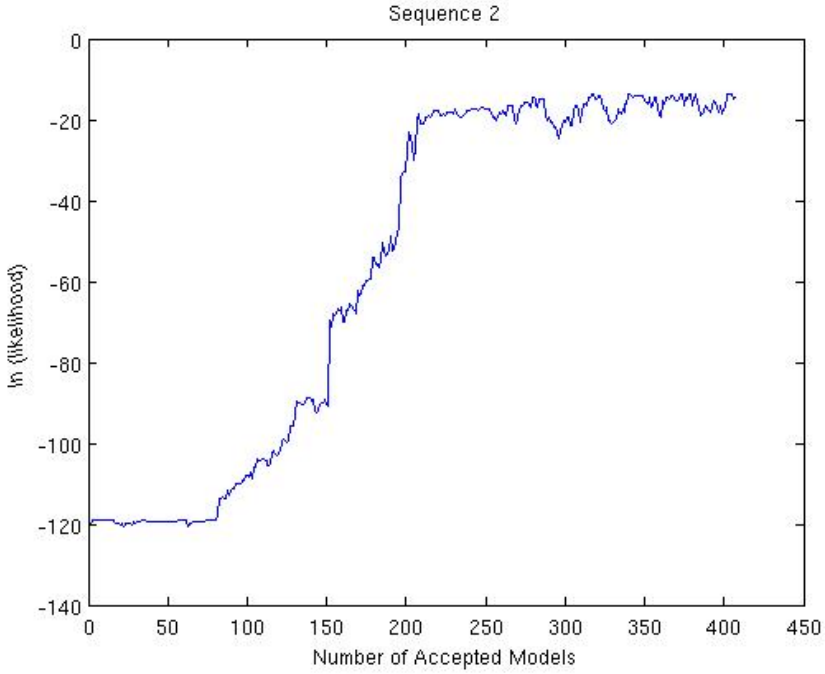

Figure 12: Plot of log likelihood versus number of models accepted into the posterior pdf showing convergence behavior of a synthetic test of the Stochastic Engine implementation.

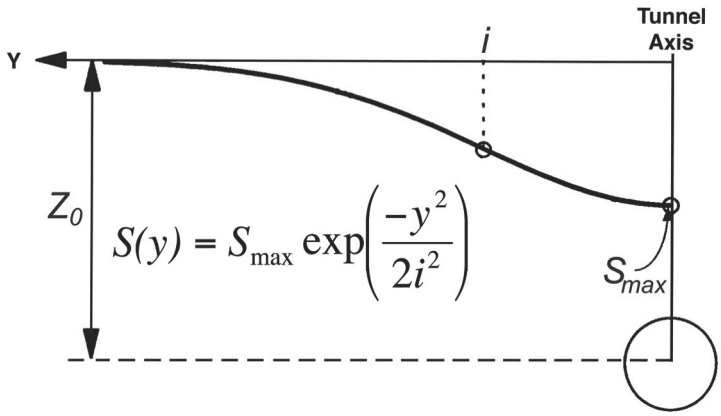

Figure 13: Vertical displacement profile model perpendicular to tunnel axis (Peck, 1969)

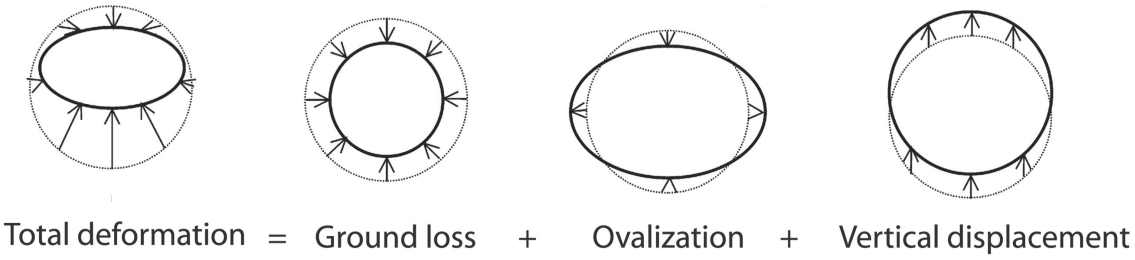

Figure 14: Deformation modes of a circular tunnel in a medium pre-stressed under gravity

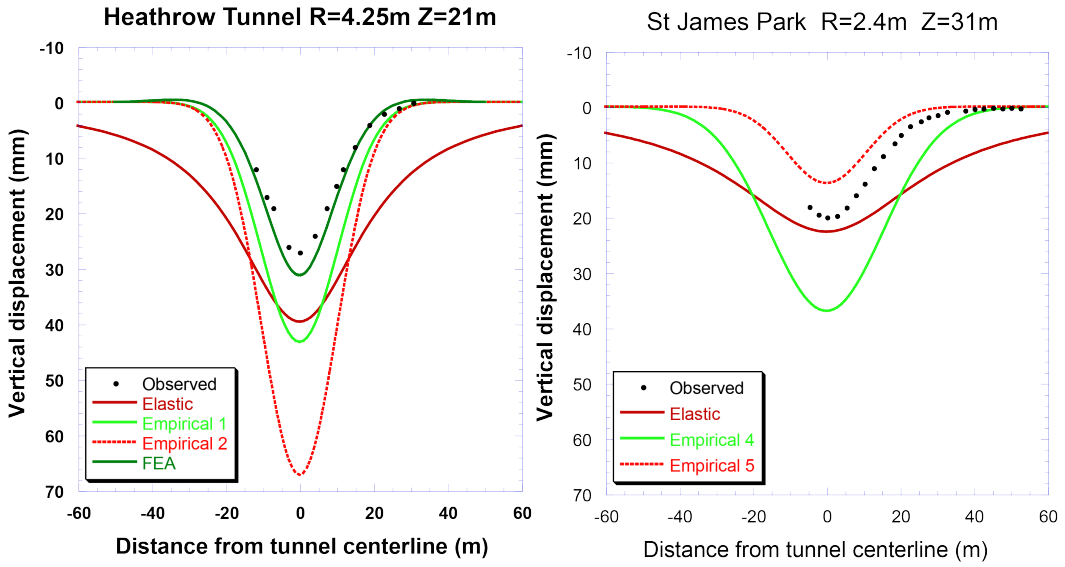

Figure 15: Comparison of vertical displacements measured perpendicular to the axes of the Heathrow Express trial tunnel (*left*) and St. James Park underground extension (*right*) with profiles calculated using different models.

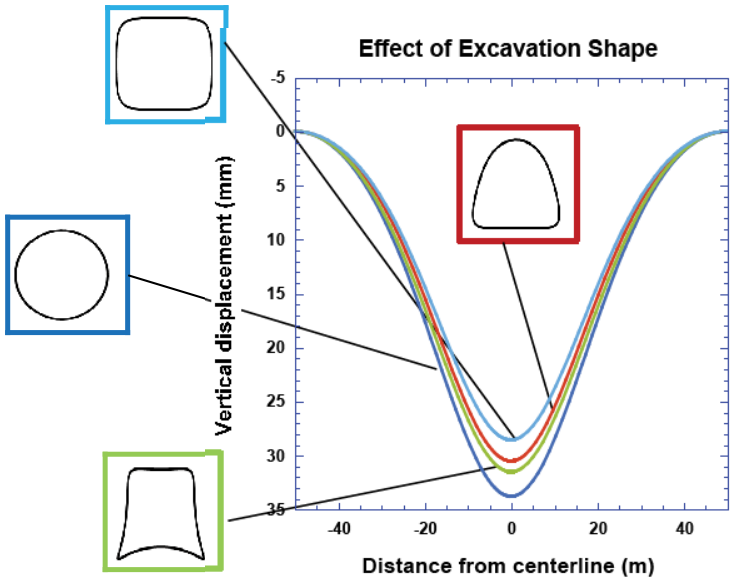

Figure 16: Finite element calculations showing the effect of tunnel cross-sectional shape on surface vertical displacements.

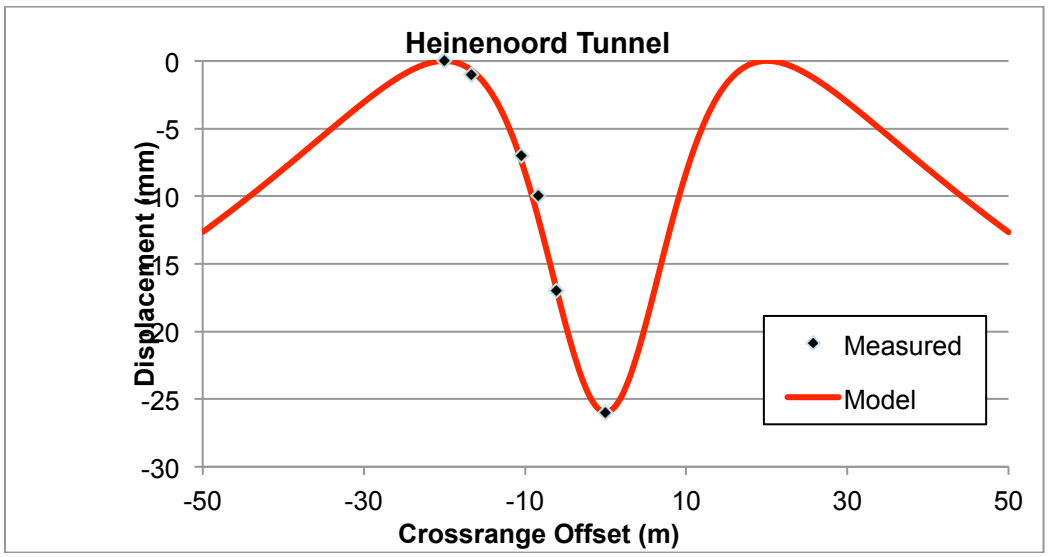

Figure 17: Vertical displacements calculated using the 3D elastic solution compared with measurements above the Heinenoord Tunnel. Model displacements are relative to maximum uplift.

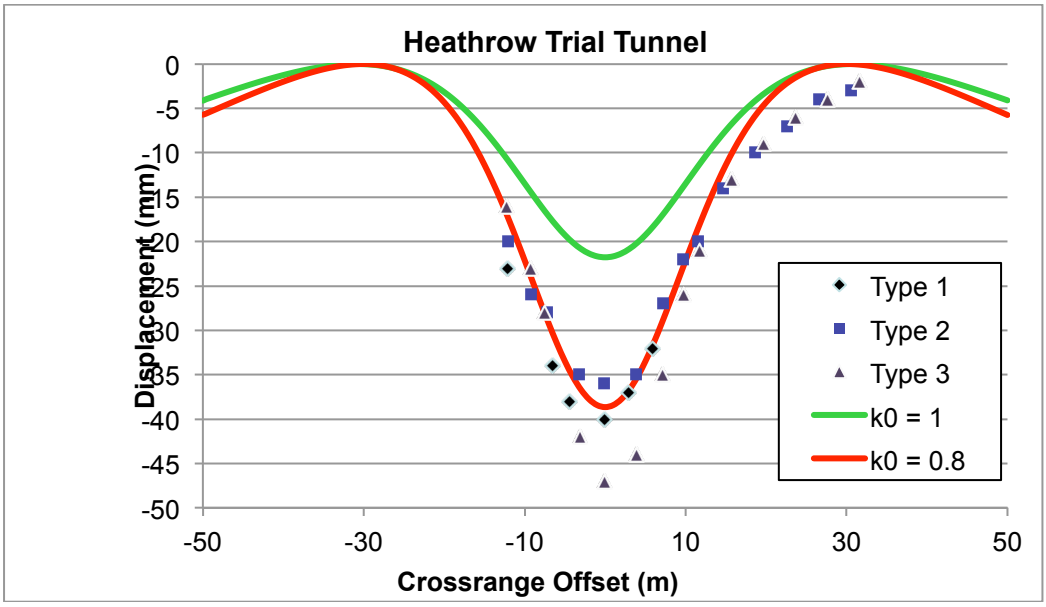

Figure 18: Vertical displacements calculated using the 3D elastic solution compared with measured profiles at three sites along the Heathrow Express trial tunnel at which different tunneling methods were employed. Model displacements are relative to maximum uplift.

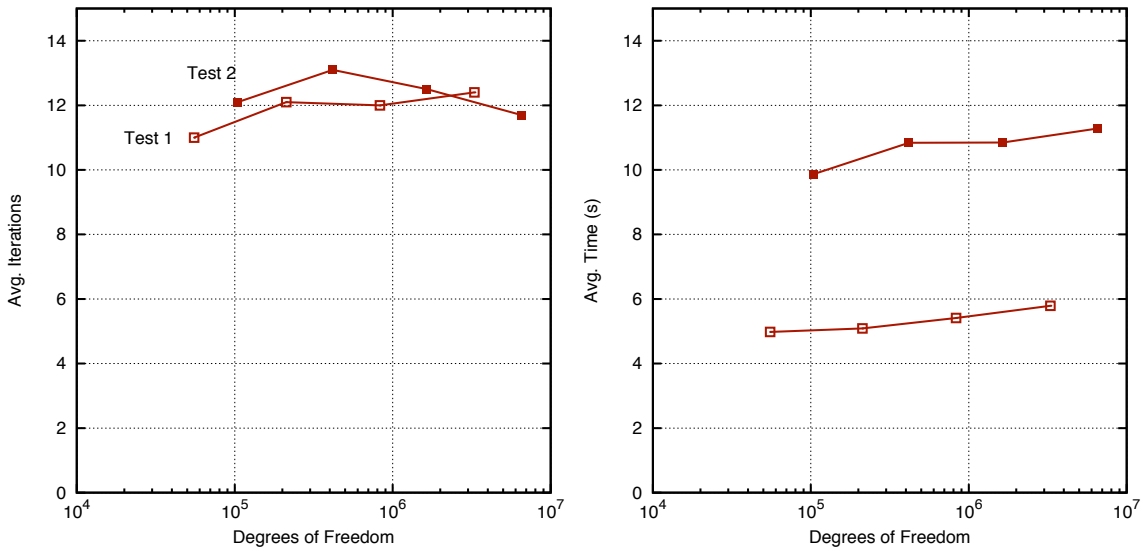

Figure 19: Poroelastic model runs demonstrating GEOCENTRIC scaling for (symbols left to right) 1, 4, 16, and 64 processors. Average number of iterations (*left*) and wall clock time (*right*) versus degrees of freedom in the model.

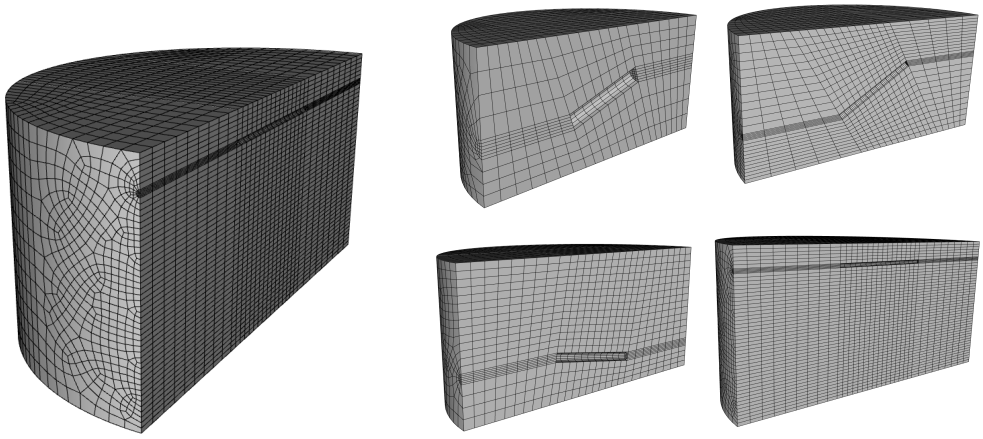

Figure 20: Finite element meshes automatically generated by CUBIT for a sequence of tunnel realizations.

Appendix A

The Stochastic Engine

The Stochastic Engine is LLNL's implementation of a Bayesian Markov Chain-Monte Carlo (MCMC) inversion scheme employing Metropolis importance-based sampling. The inversion combines existing knowledge of the bounds of model parameters and other constraints with information contained in observed data to narrow the range of possible models that are consistent with both. Existing knowledge is expressed in prior probability density functions. The solution of the inverse problem is a probability density function (pdf) over the model space. This pdf gives the relative probabilities of alternative models and therefore provides a comprehensive description of model uncertainty.

The inversion procedure (Figure A1) is initialized with a starting trial model, or "trial state". This first source model is perturbed according to a set of rules contained in the "base representation" (see below) to generate a new trial configuration, x^1. This is run through a geomechanical forward model to synthesize a set of predicted surface displacements. The likelihood $L(x^1)$ that this trial model represents the true configuration of the excavation is calculated from the fit of the predicted data to the observations according to a function of the form:

$$L(x) = k \exp\left[-\frac{1}{N} \sum_{i=1}^{N} \frac{\left| d_i^p - d_i^o \right|^n}{\sigma_i^n} \right],$$

where N is the number of observations, d^p and d^o are the predicted and observed data, respectively, σ_i is the data uncertainty and $n \geq 1$; $n=2$ (i.e. L2 norm) in the present application. From this likelihood a probability is calculated according to the Metropolis scheme:

$$\begin{aligned} P_a &= 1 && L(x^{T+1}) > L(x^T) \\ &= \frac{L\left(x^{T+1}\right)}{L\left(x^T\right)} && L(x^{T+1}) \leq L(x^T) \end{aligned}$$

where x^{T+1} and x^T are the current and last accepted state (see below), respectively. This probability is compared with a number R randomly generated in the interval 0-1. If $P_a=1$, i.e. the likelihood of the current trial is greater than the likelihood of the last *accepted* model, then the current trial model is always accepted and passed, along with its likelihood, to the posterior pdf. If $P_a > R$ the trial is also accepted. In both of these cases, the base sampler perturbs the current state to generate a new configuration and the process is repeated. Otherwise, the current trial is rejected and a new trial is generated by perturbing the last accepted model. This procedure is repeated typically for thousands to tens of thousands of trial models.

The Metropolis algorithm performs importance sampling in that it tends to "hover" in high likelihood regions of the model space, but the randomness introduced by the R parameter allows excursions to lower likelihood regions to satisfy the global search requirement. The sampling is Markovian because the process has no memory beyond the last accepted state. The MCMC procedure is guaranteed to converge to the unique,

invariant limiting posterior distribution from any starting trial model, provided that there are sufficient steps (trials) in the Markov chain.

Appropriate representation and efficient sampling of the entire range of possible models consistent with prior information are the key requirement for successful application of the SE. The base representation (Figure A1) contains the basic building blocks needed to build source model proposals (states), and the model parameter (uncertainty) pdfs and other prior constraints on the model space. The sampler contains the rules for generating the next state by perturbing the current one, consistent with a Markov process. The design of the base representation and sampler are specific to each application.

Existing forward modeling codes (written in any programming language) communicate with the SE core through specifically designed interfaces that enable the SE to pass trial sources to the forward code and receive calculated data back. The SE core and the interfaces are written in Python.

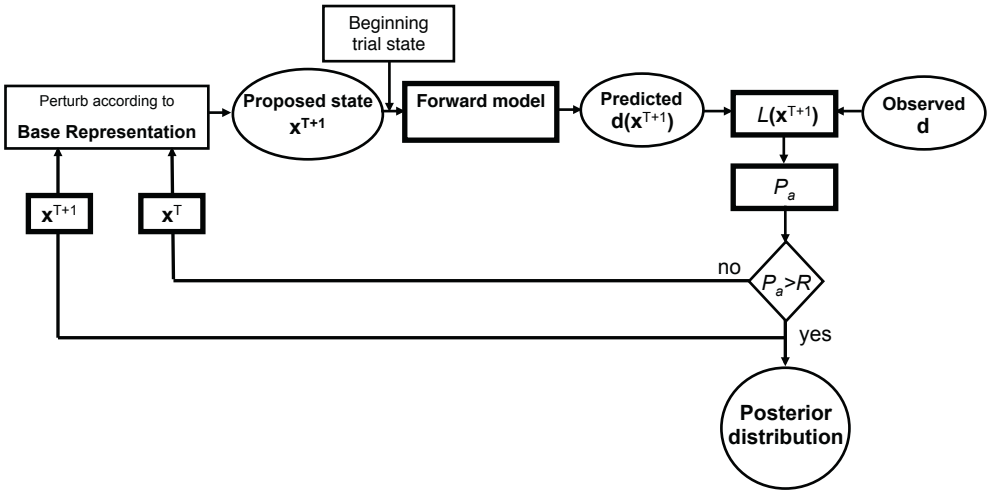

Figure A1: Schematic of the Stochastic Engine procedure

APPENDIX B

Tunneling Project Specifications

Green Park Subway

A. Tunnel Location and Geometry

The Green Park Underground tunnel is located in London, UK. The circular tunnel had an excavated diameter of 4.146 m and an axis depth of 29.3 m. It was most probably constructed in the late 1960s or early 1970s. Information along one instrumented section (X) will be presented in this appendix.

B. Construction Details

The tunnel was constructed by hand with the aid of a 3.348 m long shield that had a diameter of 4.146 m and a 6.5 mm bead. The upper portion of the face was first excavated 0.6 m ahead of the hood of the shield and was then temporarily supported. The shield was then jacked forward 0.6 m and the lower portion of the face was then excavated and temporarily supported. A 0.6 m thick, 4.070 m OD seven-segment cast-iron lining was erected in the tailskin of the shield. Concurrently, a water-cement grout was injected into the gap between the last completed tunnel lining and the excavated clay surface. The physical gap would have been equal to the size of the bead (6.5 mm) plus the difference between the excavated surface and the lining outer diameter (76 mm). However, grouting would have reduced the actual gap to at least the size of the bead. The reported ground loss was 1.3%. The rate of advance under instrumented section X was 4.5 m/day.

C. Geologic Medium

The tunnel was constructed in stiff, fissured, heavily overconsolidated London clay that is overlain by several meters of sand and gravel, most probably belonging to the Terrace Gravel geologic formation. At the time of excavation, S_u was determined to be 266 kPa at the tunnel axis level and the unit weight (γ) of the London Clay was measured to be between 18.8 - 19.9 kN/m^3. A K_0 value of 1.65 at the tunnel axis was assumed. Few other geotechnical measurements were taken at the time of excavation. Therefore, general material parameters of the Terrace Gravel and London Clay are also presented in this section.

BOREHOLE NAME	THICKNESS OF SAND AND GRAVEL LAYER (m)
X1	3.6
X2	3.0
X3	2.4

Table A3.1
Thickness of sand and gravel layer which overlays the London Clay at 8 borehole locations.

PARAMETER	TERRACE GRAVEL	LONDON CLAY
Bulk unit Weight [γ] (kN/m^3)	19 -20 (20)	18 – 20.5 (20)
Drained Young's Modulus [E'] (MPa)	30 – 160 (6*h*) *h = absolute depth below ground surface*	6*h* *h =absolute depth below ground surface*
Drained Poisson's Ratio [ν']	(0.2)	(0.2)
Drained Cohesion [c'] (kPa)	0	0 – 12 (5)
Drained Friction Angle [ϕ'] (°)	32 – 40 (35)	24 – 28 (25)
Undrained Shear Strength [S_u] (kN/m^2)	N/A	50 + 8*z* *z = depth below top of layer*
Undrained Young's Modulus [E_u] (MN/m^2)	N/A	-
Coefficient of Permeability [k] (m/s)	5 x 10^{-3} to 5 x 10^{-6}	1 x 10^{-8} to 1 x 10^{-10}
Coefficient of Earth Pressure at Rest [K_0]	0.35 – 0.5	0.8 – 2.0
Natural moisture content (%)	25 – 28	20 – 30
Liquid Limit [LL] (%)	70 – 80	54 – 85
Plastic Limit [PL] (%)	27 – 33	20 – 30
Plasticity Index [PI]	-	25 – 50
Liquidity Index [LI]	-	-0.2 – 0.2

Table A3.2
General material parameters of Terrace Gravel and London Clay. Included in parenthesis are the material parameters used for a study in nearby St. James' Park for the same geologic layers.

D. Measured Deformation Data

BOREHOLE NAME	DISTANCE FROM TUNNEL CENTERLINE (m)	VERTICAL SURFACE DEFORMATION (mm)	TIME OF MEASUREMENT (days)
X1	0.85	-4.9	21.5
X2	3.80	-4.5	16.7
X3	6.44	-3.8	19.7
X3	6.44	-4.9	23.9

Table A3.3
Short-term vertical surface deformation measurements perpendicular to the tunnel axis at instrumented section X (from Attewell and Farmer, 1974). The time of measurement refers to the time after construction under the instrumented section began, assuming an average rate of advance and incorporating known stoppage times. The measurement at X3 at 19.7 days may be an outlier. Negative vertical deformation indicates subsidence.

E. References

Addenbrooke, T.I., Potts, D.M., and Puzrin, A.M., 1997. The influence of pre-failure soil stiffness on the numerical analysis of tunnel construction, Géotechnique, 47(3), 693 – 712.

Attewell, P.B., and Farmer, I.W., 1974. Ground deformations resulting from shield tunnelling in London clay, Can. Geotech. J., 11(3), 380-395.

Burland, J.B., Jardine, F.M., and Standing, J.R., 2001. Building response to tunnelling: Case studies from construction of the Jubilee Line Extension, London. London: Thomas Telford Ltd.

Lo, K.Y., Ng, M.C., and Rowe, R.K., 1984. Predicting settlement due to tunnelling in clays. Proc. GEOTECH '84 on Tunnelling in Soil and Rock. Lo, K.Y. (ed). New York: ASCE, 46- 76.

Rowe, R.K., and Lee, K.M., 1992. Subsidence owing to tunnelling. II. Evaluation of a prediction technique, Can. Geotech. J., 29, 941-954.

St. James' Park Subway

A. Tunnel Location and Geometry

The St. James' Park Subway forms part of the Jubilee Line Extension of the London Underground in London, UK. This appendix will focus on one instrumented section above the westbound tunnel, which was constructed in April 1995. The westbound tunnel was excavated first and can be considered a greenfield site. The excavated diameter of the circular tunnel was 4.85 m. The depth to the tunnel axis is 31 m. This is a greenfield site.

B. Construction Details

The tunnel was constructed using a 4.85 m diameter, 4.2 m long open face shield and a mechanical backhoe. The maximum reach of the backhoe ahead of the shield is 1.9 m. There was a fixed bead on the shield that increased the excavated diameter 3 mm at the shield invert, 9 mm at the shield spring line, and 13 mm at the shield crown. The tunnel was lined with a 200 mm thick segmented concrete liner. Each liner ring was composed of 10 segments of 1 m width. Depending on the location of the key segments, the finished liner outer diameter could fall in the range of 4.825 m – 4.875 m. The standard size was 4.85 m. The ring build area was directly behind the tail of the shield under the cover of trailing fingers that prevented material from falling into the build area from the excavated tunnel walls. The reported volume loss was 3.3% and the reported rate of advance was 45 m/day.

C. Geologic Medium

GEOLOGIC LAYER	DEPTH (m)
Surface / Made Ground	0.0 m
Alluvium	-2.0 m
Terrace Gravels	-4.1 m
London Clay	-9.0 m
Lambeth Group	-41.5 m

Table A6.1
Geologic cross-section at a borehole 100 m from instrumented section.

PARAMETER	MADE GROUND	ALLUVIUM
Bulk unit Weight [γ] (kN/m^3)	(15 – 19)	γ_{dry} = 18 γ_{sat} = 20 (16 – 20)
Angle of Dilation [μ'] (°)	N/A	N/A
Drained Cohesion [c'] (kPa)	N/A (0)	N/A (N/A)
Drained Friction Angle [ϕ'] (°)	N/A (22 – 35)	N/A (22 – 30)
Drained Young's Modulus [E'] (MPa)	(3 – 25)	5 ($0.9E_u$)
Drained Poisson's Ratio [ν']	(-)	0.3
Undrained Young's Modulus [E_u] (MPa)	(5 – 30)	(5 – 15)
Undrained Shear Strength [S_u] (kN/m2)	(15 – 70)	(25 – 50)
Coefficient of Permeability [k] (m/s)	(1×10^{-2} to 1×10^{-6})	*depends on type of alluvium*
Coefficient of Earth Pressure at Rest [K_0]	(0.4 – 0.6)	(0.5 – 0.8)

Table A6.2
Material parameters of made ground and alluvium layers. Values are typical of those used in the published literature. General range of values in parenthesis.

PARAMETER	TERRACE GRAVEL	LONDON CLAY	LAMBETH GROUP
Bulk unit Weight [γ] (kN/m^3)	20 (19 – 20)	20 (18 – 20.5)	20 (19 – 21)
Angle of Dilation [μ'] (°)	17.5	12.5	13.5
Drained Cohesion [c'] (kPa)	0 (0)	5 (0 – 12)	200 (0 – 15)
Drained Friction Angle [ϕ'] (°)	35 (32 – 40)	25 (24 – 28)	27 (28 – 32)
Drained Young's Modulus [E'] (MPa)	6*z* (30 – 160) *z = depth below ground surface*	6*z* *z = depth below ground surface*	6*z* *z = depth below ground surface*
Drained Poisson's Ratio [ν']	0.2	0.2	0.2
Undrained Shear Strength [S_u] (kN/m2)	(N/A)	50 + 8*y* *y = depth below top London Clay*	(100 – 400)
Coefficient of Permeability [k] (m/s)	(5×10^{-3} to 5×10^{-6})	(1×10^{-8} to 1×10^{-10})	(1×10^{-6} to 1×10^{-8})
Coefficient of Earth Pressure at Rest [K_0]	(0.35 – 0.5)	(0.8 – 2)	(1 – 1.5)

Table A6.3
Material parameters of Terrace Gravel, London Clay, and Lambeth Group. Values are typical of those used in the published literature. General range of values in parenthesis.

D. Measured Deformation Data

The westbound tunnels excavated under the instrumented section between April 27 – April 28. The measurements in Table A4.4 were taken April 30 02:40.

DISTANCE FROM TUNNEL CENTERLINE (m)	VERTICLE SURFACE DISPLACEMENT (mm)
-4.76	-18.0
-2.33	-19.4
0.00	-19.9
2.69	-19.6
5.29	-18.1
7.79	-15.9
10.19	-13.8
12.67	-11.0
15.14	-8.8
18.30	-6.5
20.00	-5.0
22.50	-3.4
25.41	-2.5
27.50	-1.8
30.00	-1.4
32.50	-1.1
35.00	-0.8
37.50	-0.6
40.00	-0.3
42.43	-0.2
45.05	-0.1
47.57	-0.2
50.00	-0.1
52.52	0.2

Table A6.4
Short-term measured surface vertical displacement perpendicular to tunnel shortly after tunnel construction. Negative vertical displacement indicates subsidence (from Nyren, 1998).

Measurements taken directly above the tunnel centerline 255 days after construction recorded an additional 5.0 mm of displacement.

E. References

Addenbrooke, T.I., Potts, D.M., and Puzrin, A.M., 1997. The influence of pre-failure soil stiffness on the numerical analysis of tunnel construction, Géotechnique, 47(3), 693 – 712.

Nyren, R., 1998. Field measurement above twin tunnel in London Clay. Ph.D. thesis, Imperial College of Science Technology and Medicine.

Nyren, R.J., Standing, J.R., and Burland, J.B., 2001. Surface displacements at St. James's Park greenfield reference site above twin tunnels through the London Clay. Building Response to Tunnelling: Case Studies from Construction of the Jubilee Line Extension, London. London: Thomas Telford Ltd., 387 – 400.

Standing, J.R., Nyren, R.J., Longworth, T.I., and Burland, J.B., 1996. The measurement of ground movements due to tunnelling at two control sites along the Jubilee Line Extension. Proc. Int. Symp. on Geotechnical Aspects of Underground Construction in Soft Ground. Mair, R.J., and Taylor, R.N. (eds.), 659 – 664.

Wongsaroj, J., Soga, K., and Mair, R.J., 2007. Modeling of long-term ground response to tunnelling under St. James's Park, London, Géotechnique, 57(1), 75 – 90. E

Heathrow Express Trial Tunnel

A. Tunnel Location and Geometry

The Heathrow Express Trial tunnel is located in London, UK, near the Heathrow Airport. This 100 m long tunnel is approximately oval shaped with a cross section approximately 7.9 m high and 9.2 m wide. The general shape of the tunnel resembles a modified elliptical opening with an axis ratio of 1:1.1. The bottom half however is slightly flatter in reality. Construction began in February 1992 and was completed in May/June 1992. The depth to tunnel axis is approximately 21 m with the depth of overburden approximately 16.8 m. Information from 3 instrumented sections will be presented in this appendix. A car park is located at the surface above the tunnel.

B. Construction Details

The 100 m long tunnel was excavated using NATM and 3 different construction sequences. The first construction sequence was a double side drift sequence (Type 1), the second was a single side drift sequence (Type 2), and the third was a crown-bench-invert face excavation (Type 3). Construction was continuous without stoppage. The reported ground loss was 1.3%.

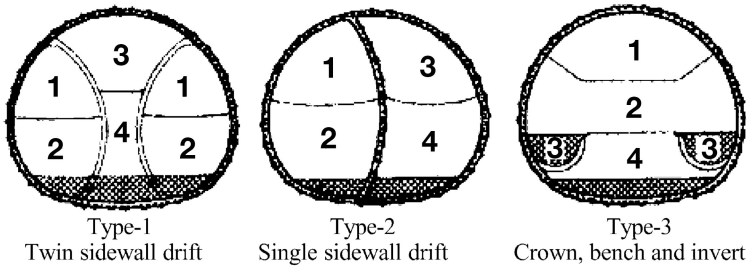

Figure A9.1
Heathrow Express Trial tunnels. Modified from Bowers [1997].

All three types were lined with an usually thick 250 mm shotcrete shell that included a single steel mesh layer and lattice girders every 1 m. Two 3 m dowels were also installed every meter at approximately 40° on either side of the crown. In mid-1994, approximately two years after the excavation ended, the invert slab was cast. In mid-1995, the cast in-situ secondary lining

was emplaced and backfilled. The tunnel would have a circular tunnel diameter equivalent of 8.5 m.

C. Geologic Medium

GEOLOGIC LAYER OR HORIZON	DEPTH (m)
Cement-stabilized materials	0.0
Course gravel	-0.3
Water table	-4.2
London Clay	-4.2

Table A9.1
Geologic cross section obtained from a vertical borehole 20 m away from access shaft.

PARAMETER	LONDON CLAY
Young's Modulus [E] (kPa)	12365
Poisson's Ratio [ν]	0.2 - 0.237
Friction Angle [ϕ] (°)	22.56
Cohesion [c] (kPa)	0
ψ (°)	11.28
G (MPa)	5
M	0.88
κ	0.066
λ	0.253
N	3.724
Unit Weight [γ] (kN/m^3)	20

Table A9.2
Material parameters of London Clay.

The material parameters of the London Clay for a linear elastic plastic Mohr-Coulomb model (E, ν, ϕ, c, and ψ) and modified Cam-Clay model (G, M, κ, λ, and N) are shown in Table A5.3.

PARAMETER	MADE GROUND	TERRACE GRAVEL
Bulk unit Weight [γ] (kN/m^3)	18 (15 – 19)	20 (19 -20)
Drained Young's Modulus [E'] (MPa)	20 (3 – 25)	20 (30 – 160)
Drained Poisson's Ratio [ν']	0.2	0.2
Drained Cohesion [c'] (kPa)	0	0
Drained Friction Angle [ϕ'] (°)	30 (22 – 35)	35 (32 – 40)
Undrained Shear Strength [S_u] (kN/m^2)	15 – 70	N/A
Undrained Young's Modulus [E_u] (MN/m^2)	5 - 30	N/A
Coefficient of Permeability [k] (m/s)	1 x 10^{-2} to 1 x 10^{-6}	5 x 10^{-3} to 5 x 10^{-6}
Coefficient of Earth Pressure at Rest [K_0]	0.4 – 0.6	0.35 – 0.5

Table A9.3
Material parameters of made ground and Terrace Gravel.

D. Measured Deformation Data

DISTANCE FROM TUNNEL CENTERLINE (m)	LONG-TERM VERTICAL SURFACE DISPLACEMENT (mm)
-12.21	-23
-6.53	-34
-4.47	-38
-0.11	-40
2.92	-37
5.90	-32

Figure A9.4
Long-term (41 - 44 months) vertical surface deformation perpendicular to tunnel axis of Type 1 tunnel (from Bowers et al., 1996).

DISTANCE FROM TUNNEL CENTERLINE (m)	SHORT-TERM VERTICAL SURFACE DEFORMATION (mm)	LONG-TERM VERTICAL SURFACE DEFORMATION (mm)
-12.03	-12	-20
-9.14	-17	-26
-7.28	-19	-28
-3.18	-26	-35
-0.11	-27	-36
3.88	-24	-
7.12	-19	-27
9.72	-15	-22
11.49	-12	-20
14.70	-8	-14
18.66	-4	-10
22.65	-2	-7
26.64	-1	-4
30.58	0	-3

Figure A9.5
Short-term (2 weeks) and long-term (41 - 44 months) vertical surface deformation perpendicular to tunnel axis of Type 2 tunnel (from Bowers et al., 1996).

DISTANCE FROM TUNNEL CENTERLINE (m)	SHORT-TERM VERTICAL SURFACE DEFORMATION (mm)	LONG-TERM VERTICAL SURFACE DEFORMATION (mm)
-12.24	-9	-16
-9.25	-15	-23
-7.50	-20	-28
-3.16	-35	-42
-0.07	-40	-47
3.92	-37	-44
7.11	-28	-35
9.71	-18	-26
11.68	-14	-21
15.71	-7	-13
19.65	-4	-9
23.71	-3	-6
27.64	-2	-4
31.65	-1	-2

Figure A9.6

Short-term (2 weeks) and long-term (41 -44 months) vertical surface deformation perpendicular to tunnel axis of Type 3 tunnel (from Bowers et al., 1996).

DISTANCE TO TUNNEL CENTERLINE (m)	MEDIUM-TERM VERTICAL SURFACE DEFORMATION (mm)
-12.14	-13
-8.99	-20
-1.61	-39
0.00	-43
3.93	-40
7.26	-32
9.97	-22
15.96	-10
19.90	-6
31.80	-1

Figure A9.7
Medium-term (13 months) vertical surface deformation perpendicular to tunnel axis of Type 3 tunnel (from New and Bowers, 1994).

E. References

Bowers, K.H., Hiller, D.M., and New, B.M., 1996. Ground movement over three years at Heathrow Express Trial Tunnel. Proc. Int. Symp. on Geotechnical Aspects of Underground Construction in Soft Ground. Mair, R.J., and Tailor, R.N. (eds.), 647 - 652.

Burland, J.B., Jardine, F.M., and Standing, J.R., 2001. Building response to tunnelling: Case studies from construction of the Jubilee Line Extension, London. London: Thomas Telford Ltd.

Cheng, C.Y., Dasari, G.R., Chow, Y.K., and Leung, C.F., 2007. Finite element analysis of tunnel-soil-pile interaction using displacement controlled model, Tunn. Underg. Space Tech., 22, 450 - 466.

Dasari, G.R., Rawlings, C.G., and Bolton, M.D., 1996. Numerical modeling of a NATM tunnel construction in London Clay. Proc. Int. Symp. on Geotechnical Aspects of Underground Construction in Soft Ground. Mair, R.J., and Taylor, R.N. (eds). Rotterdam: Balkema, 491 - 496.

Karakus, M., 2007. Appraising the methods accounting for 3D tunneling effects in 2D plane strain FE analysis, Tunn. Underg. Space Tech., 22, 47-56.

Karakus, M., and Fowell, R.J., 2003. Effects of different tunnel face advance excavation on the settlement by FEM, Tunn. Underg. Space Tech., 18, 513-523.

Loganathan, N., and Poulos, H.G., 1998. Analytical prediction for tunneling induced ground movements in clays, J. Geotechnical Environ. Eng. ASCE, 124(9), 846-856.

New, B.M., and Bowers, K.H., 1994. Ground movement model validation at the Heathrow Express trial tunnel. Tunnelling '94. London: Institution of Mining and Metallurgy, 301-329.

Masin, D., and Herle, I., 2005. Numerical analyses of a tunnel in London clay using different constitutive models, Proc. Int. Symp. on Geotechnical Aspects of Underground Construction in Soft Ground. Bakker, K.J. (ed.). London: Taylor & Francis, 595-600.

Ng, C., Simons, N., and Menzies, B., 2004. A Short Course in Soil-Structure Engineering of Deep Foundations, Excavations, and Tunnels. London: Thomas Telford Ltd.

Heinenoord Tunnel

A. Tunnel Location and Geometry

TBM construction of the Heinenoord tunnels, located in the Netherlands, began in February 1997 and concluded in June 1998. This pilot project consisted of twin tunnels with a length of 945 m, parts of which were excavated below a river. The excavated diameter was 8.55 m. The depth to the circular tunnel axis is approximately 15.5 m. Information along one instrumented section will be presented in this appendix.

B. Construction Details

A shielded German Mixshield hydroshield TBM with air regulated bentonite slurry face support was employed to construct the tunnel with a gradient of 1:30. The TBM length with trailer was 60 m and weighed 400 tonnes. The cutting wheel had a diameter of 8.55 m. The tail diameter was 20 mm smaller. The face pressure was approximately 140 kN/m^2 at the crown and linearly increased to 259 kN/m^2 at the invert. The external and internal diameter of the tunnel lining is 8.30 m and 7.60 m, respectively. The tunnel lining is a prefabricated steel fiber reinforced concrete segmental ring. The rings were 0.35 m thick, 1.50 m wide, and were composed of 7 segments and a keystone. The B45 watertight concrete with 500 S reinforcing steel segments created a watertight seal. The assumed rate of advance in a pore pressure study was between 3.3 and 5 cm/min with a 75 min stand-still between rings. The volume loss was approximately 1% and appeared to be a function of the amount of injected grout at the tail. The tunnel lining had a weight, Young's modulus, and Poisson's ratio of 24 kN/m^3, 24.6 x 10^6 kN/m^3, and 0.2, respectively. Groundwater flow hampered the plastering of the bentonite slurry onto the excavation face. Pore pressure increased as the distance between the measurement point and the excavation face decreases. During stand stills, the pore pressure decreased toward hydrostatic. Grout pressure was approximately 125 kN/m^2 at the crown increasing to 190 kN/m^2 at the invert.

C. Geologic Medium

DEPTH (m)	GEOLOGIC LAYER OR HORIZON
0.00	Surface / Fill
-1.50	Water table
-4.00	Sand
-23.25	Clay with local parts of sand

Table A8.1
Geologic cross-section at instrumented section.

In reality, the thick sand layer is a composite of four slightly different layers, but here the values have been averaged over the four layers and are treated as one layer. The ground is generally extremely soft and unstable.

PARAMETER	FILL	SAND	CLAY
Saturated Unit Weight [γ_{sat}] (kN/m^3)	17.2	20	20
Young's modulus [E] (MPa)	5.5	27	11
Drained Cohesion [c'] (kPa)	3	0	7
Drained Friction Angle [ϕ'] (°)	27	35	31
Coefficient of Earth Pressure at Rest [K_0]	0.58	0.47	0.55
Unsaturated Unit Weight [γ] (kN/m^3)	16.5	19.9	20
Poisson's Ratio [ν]	0.34	0.3	0.32

Table A8.2
Material parameters of fill, sand, and clay layers.

D. Measured Deformation Data

Measurements taken at several ring sections show that the tunnel lining crown tends to move downward between 3 and 6 mm, the invert moves up between 0 and 3 mm, and the sides displace outward between 2 and 4 mm.

DISTANCE FROM TUNNEL CENTERLINE (m)	VERTICAL SURFACE DEFORMATION (mm)
-19.97	0.0
-16.72	-1
-10.41	-7
-8.41	-10
-6.19	-17
0.00	-26

Table A8.3
Short-term vertical surface deformation measurements at instrumented section 33 m behind the excavation face (from Möller and Vermeer, 2008).

E. References

Bakker, K.J., 1999. Modelling tunnel behavior for soft soil conditions: Models for structural analysis and monitoring results. Proc. Beyond 2000 In Computational Geotechnics: 10 Years of PLAXIS International, Brinkgreve, R.B.J., (ed.). Balkema: Rotterdam, 113 – 131.

Bezuijen, A., 2004. Influence of pore pressure at tunnel face. BAW-Workshop: Boden- und Sohl-Stabilität – Betrachtungen an der Schnittstelle zwischen Geotechnik und Wasserbau, 5-1 – 5-8.

Bezuijen, A., and Talmon, A.M., 2006. Calculation models based on monitoring during tunnel construction, Tunnel. Underg. Space Tech., 21, 380 – 381.

Broere, W., 2003. Influence of excess pore pressures on the stability of the tunnel face. (Re)Claiming the Underground Space. Saveur, J. (ed.). Balkema: Rotterdam, 759 – 765.

Broere, W., and Brinkgreve, R.B.J., 2002. Phased simulation of a tunnel boring process in soft soil. Proc. 5th European Conf. Numerical Methods in Geotechnical Engineering. Mestat, P. (ed.), Paris: Presses de l'ENPC, 529 – 536.

Elkadi, A.S., and Huisman, M., 2002. 3D-GSIS geotechnical modelling of tunnel intersection in soft ground: the Second Heinenoord Tunnel, Netherlands. Tunn. Underg. Space Tech., 17, 363 -369.

Möller, S.C., and Vermeer, P.A., 2008. On numerical simulation of tunnel installation. Tunn. Underg. Space Tech., 23, 461 – 475.

Appendix C

A Three-dimensional solution for Elastic Stresses and Displacements Near a Tunnel

Overview

In this appendix we derive a surprisingly simple analytic expression for the displacement of the ground surface due to the construction of a tunnel and compare it with measurements. First, we review some elements of linear elastic theory as applied to a three-dimensional geologic medium, and in particular its response to an excavation. It is straightforward to determine approximations to the perturbed displacement and stress fields around the excavation using the harmonic potential method of Papkovitch and Neuber (see Sokolnikov, 1956, 328-335). Furthermore, we have found a simple correction scheme for these potentials to satisfy the null-stress boundary condition at the free surface of an homogeneous elastic half-space. This leads to the desired analytic expression for the surface displacements. The displacement solution is well-behaved everywhere but displays too much upthrust, or heave, due to the tunnel's buoyancy to be entirely physical. Even so, the shape of the trough in the displacement above the tunnel is in good agreement with observations. Finally, we discuss the shortcomings in our analysis that have probably led to the excess heave.

The Navier Equations

Let $\mathbf{X_0}$ be a point in an isotropic medium free of stresses. Suppose that the material is displaced by a shift to a new point $\mathbf{X}$, with displacement vector:

$$\mathbf{\Delta = X - X_0} \tag{1}$$

(To facilitate scaling, quantities with physical dimensions are indicated by upper case; dimensionless or scaled quantities by lower case, except for familiar quantities ρ, g, and the Lamé stress moduli μ, λ.)

Whether the displacement constitutes a deformation, as opposed to a simple bulk motion is indicated by the strain tensor **e,** which, for sufficiently small changes in displacement is linear in $\mathbf{\Delta}$. For rectangular coordinates with subscripts i, k, etc. indicating one of {X, Y, Z}:

$$e_{ik} = \tfrac{1}{2} (\Delta_{i,k} + \Delta_{k,i}) \tag{2}$$

where repeated derivatives imply summation and the comma denotes a partial derivative. This relation assumes the displacement changes relatively slowly with distance: $e_{ik} << 1$. Hook's law supposes a linear relation between strain **e** and stress **S**. If this relation is isotropic, it is governed by the two Lamé stress moduli μ and λ:

$$S_{ik} = 2\mu\, e_{ik} + \lambda\, e_{jj}\, \delta_{ik} \tag{3}$$

where δ_{ik} is the Kronecker delta.

The proportionality between μ and λ is described by Poisson's ratio $\nu = \lambda/(2\mu+2\lambda)$, so that

$$S_{ik}/2\mu = e_{ik} + [\nu/(1-2\nu)]\ e_{jj}\, \delta_{ik} \tag{4}$$

These linear relations among **Δ, e, S** are termed the Navier equations.

Stresses and displacements near a buried structure

Consider a uniform heavy medium with a planar geometry. This will be our 'background' prior to the excavation, denoted ($_B$). Hydrostatic equilibrium demands that the (upward) elastic force on a unit volume $F_z = S_{zk,k}$ balances its (downward) weight $W_z = \rho g$, with Z the depth. If the density ρ is uniform in a non-deformed medium, it will increase with depth from its surface value ρ_S due to compression. The result is

$$S_{BZZ} = -\rho_S g Z(1 - \tfrac{1}{2} e_{kk}) \; ; \qquad e_{kk} = e_{ZZ} \approx -\rho_S g Z / (\lambda+2\mu) \tag{5a}$$

$$S_{BXX} = S_{BYY} = k_0 S_{0ZZ} \; ; \qquad k_0 = \lambda/(\lambda+2\mu) = \nu/(1-\nu) \;\; \text{[see text]} \tag{5b}$$

k_0 is termed the 'lateral stress coefficient', which is the ratio of the vertical to the horizontal stress. Although we evaluate it here for a uniform elastic medium, it can be influenced significantly by geologic factors apart from elasticity. Hence, we treat k_0 and ν as independent parameters.

Note that linear theory requires that $|e_{kk}| << 1$. Nominal parameters of soft soil might be ρ_0=2000 kg/m^3, μ=5 MPa, ν=0.2, for which $|e_{kk}| << 1$ implies Z << 1 km. For structures at depths of tens of meters e_{kk} in (5a) is negligible and will be ignored here; thus $\rho \approx \rho_S$, $S_{BZZ} \approx -\rho_S g Z$.

The presence of the excavation modifies the background stress $\mathbf{S_B}$, since the stresses on the walls surrounding a void must be zero. The total stress can be expressed as $\mathbf{S_T = S_B + S}$ such that the perturbation **S** cancels the background stress $\mathbf{S_B}$ normal to the walls. By the linearity of the Navier equations above, **S** has a related displacement **Δ** obeying (2)-(4). Thus, **Δ** measures the movement induced by the excavation relative to the initially-stressed ground. Outside the structure, $\mathbf{S_B}$ balances the weight of the ground for small displacements; thus, **S** is divergence-free, $S_{ik,k}=0$. (This condition is very useful, although not entirely valid for large structures. A modification is considered below.)

After Sokolnikoff (1956), we may write the general form for a divergence-free displacement using four harmonic potentials Ψ, Φ_i that obey Laplace's equation, $\Phi_{i,kk} = \Psi_{,kk} = 0$.

$$2\mu\Delta_i = \Psi_{,i} + X_k \Phi_{k,i} - \kappa \Phi_i \; ; \; \kappa \equiv 3-4\nu \tag{6}$$

If there is reflection symmetry in the X, Y directions, the potentials Φ_X and Φ_Y are null. In this case, with $\Phi \equiv \Phi_Z$, the displacement is

$$2\mu\Delta_i = \Psi_{,i} + Z \Phi_{,i} - \kappa \Phi \delta_{iZ} \tag{7}$$

The stress for this displacement follows from (2-4). Components are

$$S_{XX} = \Psi_{,XX} + Z\Phi_{,XX} - 2\nu\,\Phi_{,Z} \qquad \text{(Y may replace X)} \tag{8a}$$

$$S_{XZ} = \Psi_{,XZ} + Z\Phi_{,XZ} - (1-2\nu)\Phi_{,X} \qquad \text{(Y may replace X)} \tag{8b}$$

$$S_{ZZ} = \Psi_{,ZZ} + Z\Phi_{,ZZ} - (2-2\nu)\Phi_{,Z} \tag{8c}$$

$$S_{XY} = \Psi_{,XY} + Z\Phi_{,XY} \tag{8d}$$

Expanding Ψ, Φ in appropriate basis functions an approximate solution can be determined that satisfies the boundary condition at the excavation, i.e. $(\mathbf{S_0+S})\cdot\mathbf{n} = 0$, with **n** normal to the walls of the void. This gives an appropriate modification to the background stress field in the vicinity of the excavation.

Harmonic potentials near a tunnel

Figure C1 is a guide to the geometry and notation to be used in this discussion: It shows the coordinate directions (X, Y, Z); a tunnel of radius R_T at depth Z_T with ends at $\pm Y_T$; and a source point **S** along the tunnel axis and a field point **F** at arbitrary (X, Y, Z): C, R, D are useful to describe their relation.

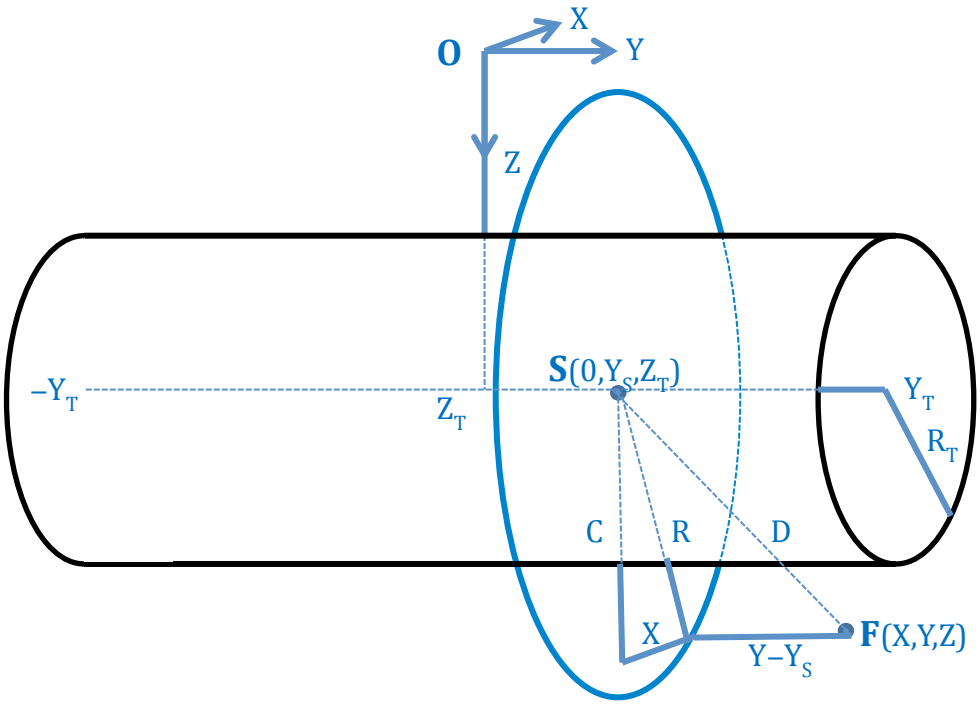

Figure C1. Nomenclature for the discussion of tunnels. Lengths are capitalized; corresponding displacements scaled by the tunnel radius are lower-case, e.g. $c \equiv C/R_T$.

We must determine potentials Ψ, Φ for a perturbation stress S that cancels the normal components of the background stress S_B on the tunnel wall. We express the potentials using a basis of dimensionless harmonic functions t_n. To express this basis as simply as possible, it is necessary to use scaled distances similar to the

physical distances indicated in the figure. The tunnel radius R_T is a convenient scale parameter. Scaled quantities are written lower case, e.g. $x = X/R_T$, $c = C/R_T = (Z–Z_T)/R_T$. On the wall $r^2 = x^2+c^2 = 1$. The boundary conditions there are

$$S_{RR}=–S_{BRR}: \quad c^2S_{ZZ} + 2xcS_{XZ} + (1–c^2)S_{XX} = [k_0+(1–k_0)\,c^2](c+z_T)\,\rho g R_T \tag{9a}$$

$$S_{\circ R}=–S_{B\circ R}: \quad xc(S_{ZZ}–S_{XX}) + (1–2c^2)S_{XZ} = (1–k_0)\,xc(c+z_T)\,\rho g R_T \tag{9b}$$

θ is the angular displacement along the wall in the x-z plane. For nominal parameters $\rho g \approx 20$ kN/m^3, $R_T \approx 4$ m and the baseline stress $\rho g R_T$ is 80 kPa.

The harmonic basis is derived from the fundamental spherical harmonic about the source point **S**:

$$h_0 = d^{-1} \qquad d^2 = x^2+(y–y_S)^2+c^2 \tag{10}$$

Stresses at the tunnel surface are independent of Y, the distance along the tunnel from its mid-plane, so we seek harmonics that share this behavior. An approximation corresponding to h_0 is

$$t_0 = \int_{-y_T}^{y_T} h_0 \, dy_S \tag{11}$$

Other harmonics follow by differentiation with respect to the vertical coordinate c:

$$t_n = t_{n-1,c} \tag{12}$$

These functions can be expressed analytically [Gradshteyn and Ryzhik, 1965, (2.26 ff)]

$$t_n(y) = ½[\tau_n(y) + \tau_n(–y)] \tag{13a}$$

$$\tau_0 = \ln[(a+\gamma)^2/r^2]; \quad \tau_1 = –2\gamma c / ar^2; \quad \tau_2 = 2\gamma\,(2b^2c^2–a^2r^2)\,/a^3r^4;$$

$$\tau_3 \approx 4\gamma c b^2(3r^2–4c^2)\,/a^3r^6; \quad \tau_4 \approx 12\gamma b^2(8c^4–8c^2r^2+r^4)\,/a^3r^8 \tag{13b}$$

$$\gamma = y_T–y; \qquad a^2 = \gamma^2+r^2 \qquad b^2 = a^2+½r^2$$

For τ_3 and τ_4, terms of $o(y_T^{-4})$ are neglected. In our scheme, the harmonic t_{-1} also appears formally, but for the stresses and vertical displacement, derivatives with respect to z always reduce it to t_0 or t_1 for evaluation.

Near the tunnel, but away from its ends (r, $|y| < y_T$), $\gamma \approx a \approx b \approx y_T$; so:

$$t_0 \approx 2\ln[2y_T/r]; \quad t_1 \approx –2c\,/r^2; \quad t_2 \approx (4c^2–2r^2)\,/r^4; \quad t_3 \approx 4c(3r^2–4c^2)\,/r^6;$$

$$t_4 \approx 12(8c^4–8c^2r^2+r^4)\,/r^8 \tag{14}$$

We refer to this as the 'central' approximation (but note that it is valid even far from the center of the tunnel).

For this approximation, coefficients in the expansions $\Psi=\Psi_n\ t_n$, $\Phi=\Phi_n\ t_n$ can be determined such that equations (9) are satisfied for the stresses (8) on the tunnel wall r=1. Both sides of (9a,b) are explicit polynomials in c; so these equations can be solved analytically by grouping similar terms. The result is

$$\Phi = (\rho g R_T^2)\ [t_0/8(1-\nu) + (1-k_0)(-z_T t_1/2 + t_2/8)] \qquad (15a)$$

$$\Psi = (\rho g R_T^3)\{[(3-4\nu)\ z_T t_0 - (1-2\nu)\ t_1/2]/8(1-\nu) +$$

$$+ (1-k_0)\ [-(5-4\nu)\ z_T t_0/4 + [z_T^2 + (3-2\nu)/4]\ t_1/2 - z_T t_2/4 + t_3/48]\} \qquad (15b)$$

Thus, there is considerable simplification for isotropic background stress $k_0=1$.

In Figure C2 we illustrate the behavior of the solution near an end, using the y-dependences of the harmonics t_n in (13). Parameters are similar to those for the Heinenrood tunnel (below). In this case, $k_0<1$, and the shear-stress in the background earth is significant.

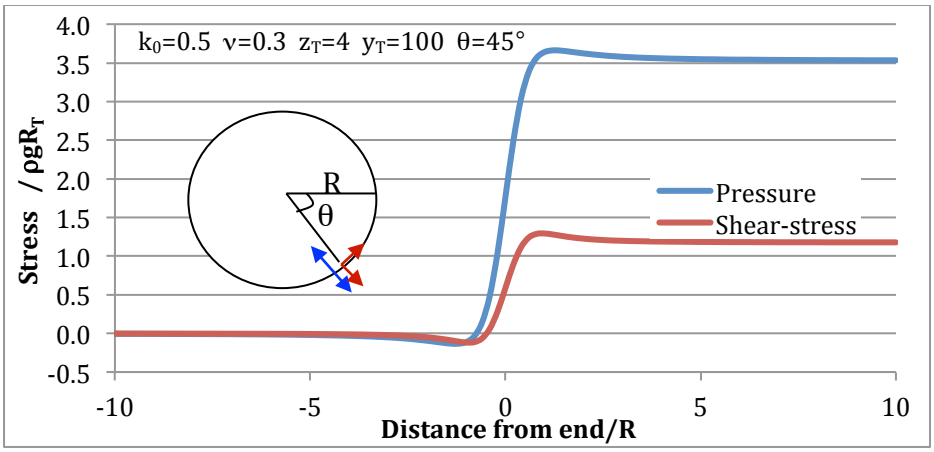

Figure C2: Total pressure $-S_{RR}$ and shear-stress $-S_{rR}$ on an element of a circular contour 45° from horizontal. Beyond the tunnel, the stresses from the exterior rock try to push the element in and up; within the tunnel, the elastic strain at the wall reduces these stresses to zero.

As seen in Figure C2, the analytic solution gives a stress that transitions from the tunnel boundary conditions (null normal stress) to those of the background rock over a relatively short distance (similar to radius, rather than depth or length) – the desired behavior. In fact, it would be difficult to do better in a simple treatment: A more exact solution in this region would depend on details of the end wall and appropriate corrections to the strengths of the sources of the potentials there. This is an important result, since it allows us to use the expansion coefficients in (15) generally, not just near the epicenter.

Potentials and stresses at the ground surface

We are particularly interested in the vertical displacement at the free surface z=0. In this section we derive analytic approximations for the displacement, which was a goal for this investigation. This follows from the values of the fields Ψ, Φ found to satisfy the boundary condition at the excavation, eq. (9a,b). However, these must be corrected to give null vertical stresses S_{iZ} at the surface. This may be done using images of Ψ, Φ reflected across the surface. These image fields will affect the stress near the excavation, but their influence will be negligible at sufficient depth.

Corrected fields Ψ', Φ' with null vertical surface stresses are

$$\Psi' = \Psi + \kappa\, \Psi_I + \beta \Phi_I^{'Z} \quad \beta \equiv 4(1-\nu)(1-2\nu) \tag{16a}$$

$$\Phi' = \Phi + \kappa\, \Phi_I + 2\, \Psi_{I,Z} \tag{16b}$$

For the image fields $\Psi_I(\mathbf{X}) \equiv \Psi(\mathbf{X_I})$, $\Phi_I(\mathbf{X}) \equiv \Phi(\mathbf{X_I})$ with $\mathbf{X_I} \equiv (X,Y,-Z)$ the image of $\mathbf{X}$. In (16a) $\Phi^{'Z}(Z) \equiv \int^Z \Phi(Z')\, dZ'$ denotes the anti-derivative, such that $\Phi^{'Z}{}_{,Z} = \Phi$.

Corresponding stresses can be computed from (3). In particular, for the vertical stresses:

$$S'_{ZZ} = \Psi_{,ZZ} - \Psi_{I,ZZ} + Z\Phi'_{,ZZ} - (2-2\nu)[\Phi_{,Z} + \Phi_{I,Z}] \tag{17a}$$

$$S'_{XZ} = [\Psi_{,Z} + \Psi_{I,Z}]_{,X} + Z\Phi'_{,XZ} - (1-2\nu)[\Phi - \Phi_I]_{,X} \tag{17b}$$

At Z=0, $\Psi_I = \Psi$ but $\Psi_{I,Z} = -\Psi_{,Z}$ (similarly for Φ_I). Therefore the stresses in (17) can be seen to vanish at the surface.

Just as Ψ, Φ die away with distance from the excavation, so Ψ_I and Φ_I die away from the image of the excavation. They will be negligible at the excavation itself if it is at sufficient depth. Figure C3 shows that even for shallow tunnels, $Z_T \sim$ 2-3 R_T, the mismatch is likely unimportant.

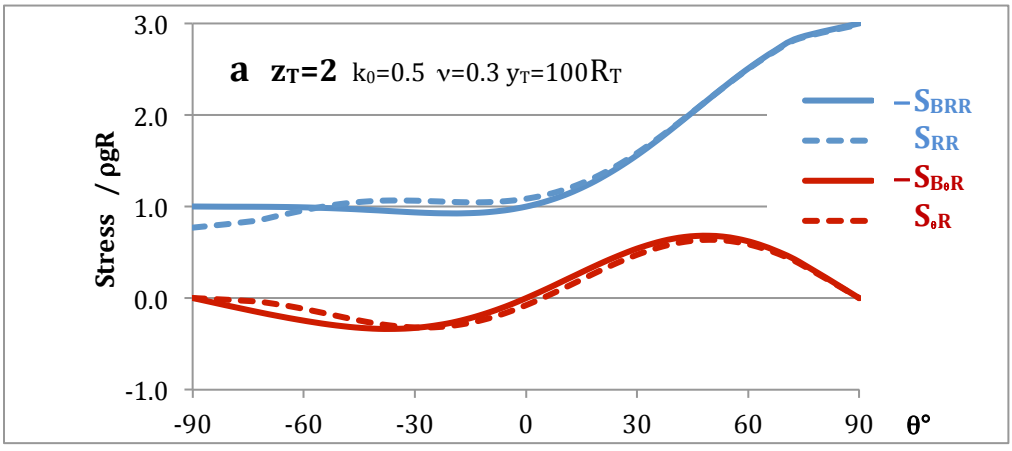

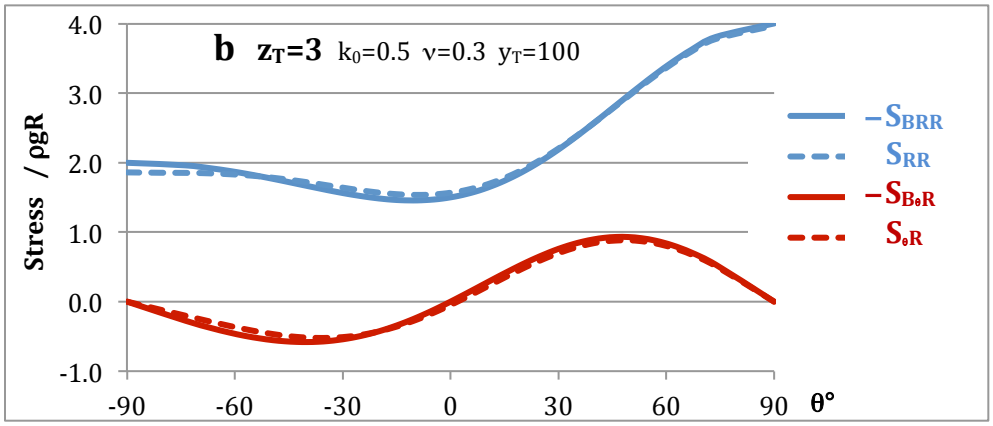

Figure C3: Mismatch due to image fields. Stresses S_{RR}, $S_{\theta R}$ due to the displacement of the tunnel wall, including the image fields, are compared to those in the background earth, $-S_{BRR}$, $-S_{B\theta R}$. The resulting mismatch is of order 10% for (a) d=2 (overburden equals tunnel radius), and 1% for (b) d=3 (overburden equals tunnel diameter).

Displacement at the ground surface

The surface displacement for the corrected fields can be found by (6). It is surprisingly simple:

$$2\mu\, \Delta`_Z(Z=0) = 4(1-\nu)\Psi_{,Z} - 8(1-\nu)^2\Phi \qquad (18)$$

Here, $\Delta`_Z$ is the displacement due to Ψ',Φ', and Ψ, Φ are the <u>original</u> fields. Note that this is a general result for buried structures.

For the tunnel, with fields as in (15), this becomes

$$\Delta`_Z(Z=0) = (\rho g R_T^2/2\mu)\{-(1-\nu)\, t_0 + \tfrac{1}{2}\kappa z_T\, t_1 - \tfrac{1}{4}(1-2\nu)\, t_2 + \\ + (1-k_0)(1-\nu)\,[-z_T\, t_1 + (2z_T^2+\tfrac{1}{2})\, t_2 - z_T\, t_3 + t_4/12]\} \qquad (19)$$

For nominal parameters $\rho g \approx 20$ kN/m^3, $R_T \approx 4$ m, $\mu \approx 5$ MPa, the baseline displacement is 8 mm.

Near the tunnel, but away from its ends, the t_n are simple functions (14); so (19) is easy to evaluate:

$$\Delta`_Z(Z=0) \approx (\rho g R_T^2/2\mu)(\delta_H + \delta_0 + \delta_2) \qquad (20)$$

$$\delta_H = -(2-2\nu)\ln(2Y_T/R)$$

$$\delta_0 = [(3-4\nu) + (1-k_0)(1-\nu)(-6+8Z_T^2/R^2)]\, Z_T^2/R^2$$

$$\delta_2 = [(1-2\nu)(\tfrac{1}{2} - Z_T^2/R^2) + (1-k_0)(1-\nu)(-1+14Z_T^2/R^2-16Z_T^4/R^4)]\, R_T^2/R^2$$

We have grouped terms by their dependence on the ratio $1/r = R_T/R$. We have neglected a term of $o(1/r^4)$, which can be shown to be entirely negligible.

Nature of the surface displacement: Equation (19) is the main result for this study, since it gives a tractable analytic form for the surface displacement produced by a tunnel. Its approximation in (20) is remarkably simple; yet we shall see that it agrees quite well with observations in simple geologies. Both expressions have the leading terms:

$$\Delta`_{ZH} = (\rho g R_T^2/2\mu)\, \delta_H \qquad (21)$$

$$\delta_H = -(1-\nu)\ln[(a_+ + \gamma_+)(a_- + \gamma_-)/r^2] \approx -(2-2\nu)\ln(2y_T/r)$$

$$\gamma_\pm = y_T \pm y; \qquad a_\pm^2 = \gamma_\pm^2 + r^2$$

This increases logarithmically with tunnel length in the central approximation ($r, |y| < y_T$), as shown. For $r >> y_T$ it does indeed go to zero, even along the axis with $y \approx r$.

This term, the upthrust or heave caused by the buoyancy of the tunnel, gives an overall displacement that may well be uniformly upward, even at the lowest point in the trough. Since this increases the gravitational potential energy, it probably reflects an incomplete treatment of the perturbation and gravitational effects, as discussed in the main body of the report. We believe this incompleteness is primarily due to the lack of a term proportional to t_{-1} in eq. (15b) for Ψ, which would have a simple correction. In any case, the heave peak is broad, and so does not affect the shape of the trough significantly, as illustrated in Figure C4.

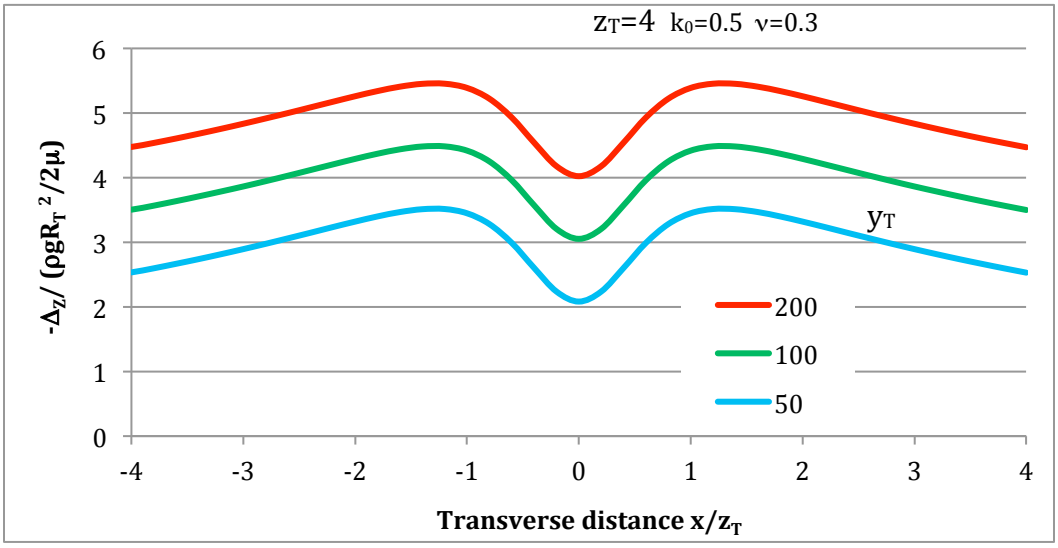

Figure C4: Heave and tunnel length. Buoyancy results in a broad peak that has little effect on the trough shape. The relative trough depth is about 1.5 the scale value, about 1.2 cm.

The empirical measurements considered below extend only to the edge of the trough produced by the tunnel. This edge presumably lies at the maximum upthrust produced by the tunnel's buoyancy. So, for comparison with measurements, we define the trough depth relative to the maximum upthrust transverse to the tunnel axis, indicated $\Delta_{Z\text{-}REL}$

Figure C5 presents the dependence of the trough shape (away from the tunnel ends, the 'central' approximation) on the parameters k_0, ν, z_T. The baseline used is similar to parameters of the Heinenrood tunnel, as in the previous figures, and only single-parameter variations are considered. If k_0 is small, there is less transverse compression from the background – the tunnel can flatten, giving a larger displacement. Similarly, if the earth can compress (small ν) the displacement is larger. Depth of burial in the range considered, $2 < z_T < 8$, has less influence on the magnitude of the displacement. However, the width of the trough is comparable to this depth; so a deep tunnel will produce a trough of larger cross section.

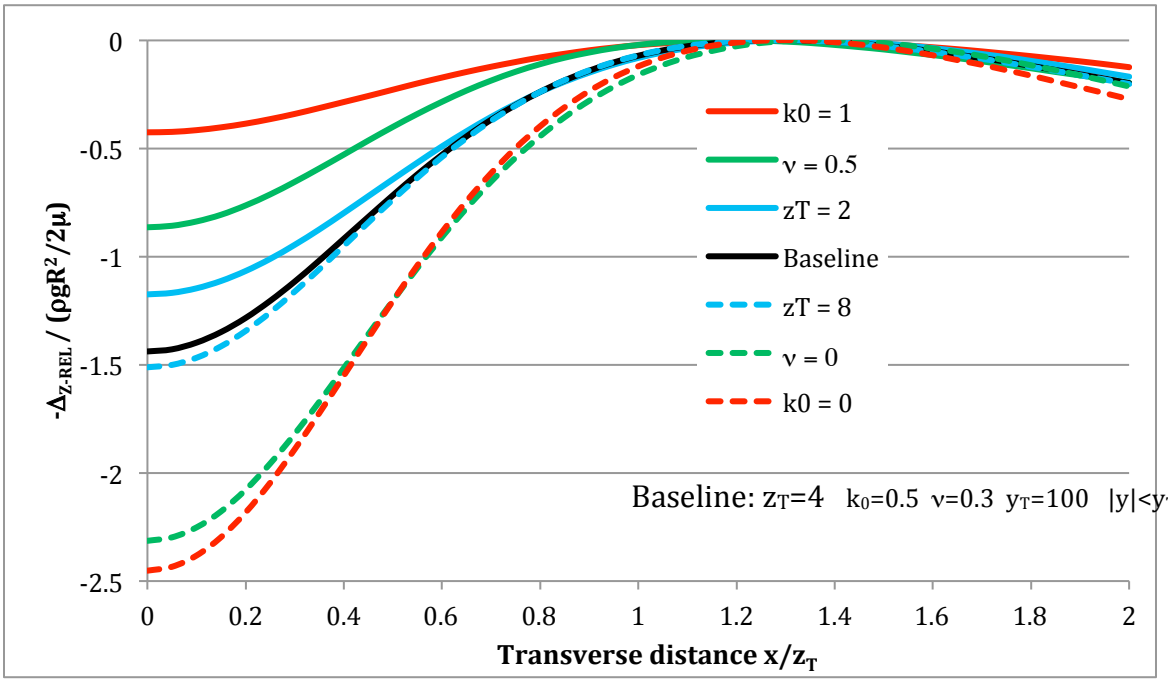

Figure C5: Trough shape as a function of k_0(red), ν(green), d(blue), for single parameter variations around the baseline of the previous figures. Depth in the trough $\Delta_{Z\text{-}REL}$ is measured relative to the maximum upthrust due to the tunnel's buoyancy.

In Figure C5 the trough width is consistently comparable to the depth of burial, $x \sim 1.25 z_T$. So it is not surprising that similar behavior is observed for the extension of the trough beyond the tunnel ends. This is shown in Figure C6, where we plot the relative trough depth $\Delta_{Z\text{-}REL}(x=0)$. At a distance beyond an end corresponding to the depth, there is no longer a trough, $\Delta_{Z\text{-}REL} \sim 0$, even though there may still be upthrust

due to buoyancy. The figure shows that the displacement is constant along most of the axis, an important result validating use of the 'central' approximation.

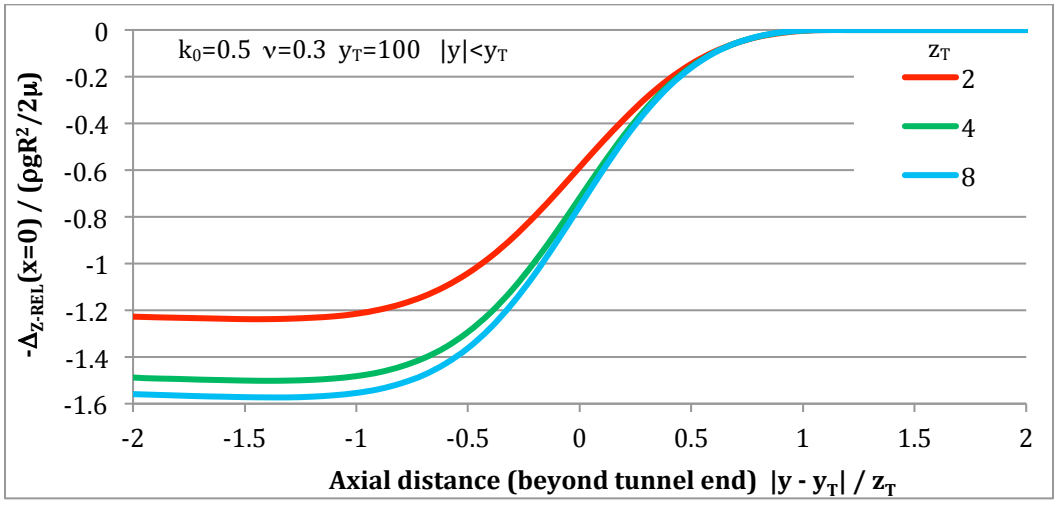

Figure C6: Central trough depth relative to maximum upthrust, as a function of axial position. At distance ~$1.25z_T$ from the end, and beyond, there is no trough – so zero trough depth – even though upthrust due to buoyancy persists. Baseline is as in the preceding figures.

REFERENCES

I. S. Gradshteyn and I. M. Ryzhik, *Tables of Integrals, Series and Products*, Academic Press, 1965.

Sokolnikoff, I.S., *Mathematical Theory of Elasticity*, McGraw Hill, 1956.